

# Changes in apparent temperature and PM<sub>2.5</sub> around the Beijing-Tianjin megalopolis under greenhouse gas and stratospheric aerosol intervention scenarios

Jun Wang<sup>1</sup>, John C. Moore<sup>1,2\*</sup>, Liyun Zhao<sup>1\*</sup>

<sup>1</sup>College of Global Change and Earth Systems Science, Beijing Normal University, Beijing 100875, China

<sup>2</sup>Arctic Center, University of Lapland, Rovaniemi, Finland

*Correspondence to:* zhaoliyun@bnu.edu.cn, john.moore.bnu@gmail.com

**Abstract.** Apparent temperatures (AP) and ground level aerosol pollution (PM<sub>2.5</sub>) are important factors in human health, particularly in rapidly growing urban centres in the developing world. We quantify how changes in apparent temperature – that is a combination of 2 m air temperature, relative humidity and surface wind speed, and PM<sub>2.5</sub> concentrations – that depend on the same meteorological factors along with future industrial emission policy, may impact people in the greater Beijing region. Four Earth System Models (ESM) simulations of the modest greenhouse emissions RCP4.5, the “business-as-usual” RCP8.5 and the stratospheric aerosol intervention G4 geoengineering scenarios are downscaled using both a 10 km resolution dynamic model (WRF), and a statistically approach (ISIMIP). We use multiple linear regression models to simulate changes in PM<sub>2.5</sub> and the contributions meteorological factors make in controlling seasonal AP and PM<sub>2.5</sub>. WRF produces warmer winters and cooler summers than does ISIMIP both now and in the future. These differences mean that estimates of numbers of days with extreme apparent temperatures vary systematically with downscaling method, as well as between climate models and scenarios. Air temperature changes dominate differences in apparent temperatures between future scenarios even more than they do at present because the reductions in humidity expected under solar geoengineering are overwhelmed by rising vapor pressure due to rising temperatures and the lower windspeeds expected in the region in all future scenarios. Compared with the 2010s, PM<sub>2.5</sub> concentration is projected to decrease 5.4 µg/m<sup>3</sup> in the Beijing-Tianjin province under the G4 scenario during the 2060s from the WRF downscaling, but decrease by 7.6 µg/m<sup>3</sup> using ISIMIP. The relative risk of 5 diseases decreases by 1.1%-6.7% in G4/RCP4.5/RCP8.5 using ISIMIP, but have smaller decrease (0.7%-5.2%) using WRF. Temperature and humidity differences between scenarios change the relative risk of disease from PM<sub>2.5</sub> such that G4 results in 1-3% higher health risks than RCP4.5. Urban centres see larger rises in extreme apparent temperatures than rural surroundings due to differences in land surface type, and since these are also the most densely populated, health impacts will be dominated by the larger rises in apparent temperatures in these urban areas.

41 **500 character non-technical text**

42 Apparent temperatures and PM<sub>2.5</sub> pollution depends on humidity and wind speed in  
43 addition to surface temperature and impacts human health and comfort. Apparent  
44 temperatures will reach dangerous levels more commonly in future because of water  
45 vapor pressure rises and lower expected wind speeds, but these will also drive change  
46 in PM<sub>2.5</sub>. Solar geoengineering can reduce the frequency of extreme events significantly  
47 relative to modest, and especially “business as usual” greenhouse scenarios.

48  
49  
50 **1. Introduction**

51 Global mean surface temperature has increased by 0.92°C (0.68-1.17°C) during 1880-  
52 2012 (IPCC, 2021), which naturally also impacts the human living environment  
53 (Kraaijenbrink et al., 2017; Garcia et al., 2018). However, neither land surface  
54 temperature nor near-surface air temperature can adequately represent the temperature  
55 we experience. Apparent temperature (AP), that is how the temperature feels, is  
56 formulated to reflect human thermal comfort and is probably a more important  
57 indication of health than daily maximum or minimum temperatures (Fischer et al., 2013;  
58 Matthews et al., 2017; Wang et al., 2021). There are various approaches to estimating  
59 how the weather conditions affect comfort, but apparent temperature is governed by air  
60 temperature, humidity and wind speed (Steadman 1984; Steadman 1994). These are  
61 known empirically to affect human thermal comfort (Jacobs et al., 2013), and thresholds  
62 have been designed to indicate danger and health risks under extreme heat events (Ho  
63 et al., 2016). Analysis of historical apparent temperatures in China (Wu et al., 2017; Chi  
64 et al., 2018; Wang et al., 2019), Australia (Jacobs et al., 2013), and the USA (Grundstein  
65 et al., 2011) all find that apparent temperature is increasing faster than air temperature.  
66 This is due to both decreasing wind speeds and, especially to increasing vapor pressure  
67 (Song et al., 2022).

68  
69 As the world warms, apparent temperature is expected to rise faster than air  
70 temperatures in the future (Li et al., 2018; Song et al., 2022). Hence, humans, and other  
71 species, will face more heat-related stress but less cold-related environmental stress in  
72 the warmer future (Wang et al., 2018; Zhu et al., 2019). Since most of the population is  
73 now urban, the conditions in cities will determine how tolerable are future climates for  
74 much of humanity, while the differences in thermal comfort between urbanized and  
75 rural regions will be a factor in driving urbanization. Reliable estimates of future urban  
76 temperatures and their rural surroundings require methods to improve on standard  
77 climate model resolution to adequately represent the different land surface types;  
78 especially the rapid and accelerating changes in land cover in the huge urban areas  
79 characteristic of sprawling developments in the developing world. This is usually done  
80 with either statistical or dynamic downscaling approaches, and in this article we  
81 examine both methods.

82  
83 In early 2013, Beijing encountered a serious pollution incident. The concentration of  
84 PM<sub>2.5</sub> (particles with diameters less than or equal to 2.5 μm in the atmosphere) exceeded  
85 500 μg/m<sup>3</sup> (Wang et al., 2014). Following this event and its expected impacts on human  
86 health (Guan et al., 2016; Fan et al., 2021) and the economy (Maji et al., 2018; Wang  
87 et al., 2020), the Beijing municipal government launched the Clean Air Action Plan in  
88 2013. The annual mean concentration of PM<sub>2.5</sub> in Beijing-Tianjin-Hebei region  
89 decreased from 90.6 μg/m<sup>3</sup> in 2013 to 56.3 μg/m<sup>3</sup> in 2017, a decrease of about 38%  
90 (Zhang et al., 2019), although this is still more than double the EU air quality standard  
91 (25 μg/m<sup>3</sup>) and above the Chinese FGNS (First Grand National Standard) of 35 μg/m<sup>3</sup>.  
92 The concentration of PM<sub>2.5</sub> is related to anthropogenic emissions, but also dependent  
93 on meteorological conditions (Chen et al., 2020). Simulations suggested that 80% of  
94 the 2013-2017 lowering of PM<sub>2.5</sub> concentration came from emission reductions in  
95 Beijing (Chen et al. 2019). Humidity and temperature are the main meteorological  
96 factors affecting PM<sub>2.5</sub> concentration in Beijing in summer, while humidity and wind  
97 speed are the main factors in winter (Chen et al., 2018). Simulations driven by different  
98 RCP emission scenarios with fixed meteorology for the year 2010 suggest that PM<sub>2.5</sub>  
99 concentration will meet FGNS under RCP2.6, RCP4.5 and RCP8.5 in Beijing-Tianjin-  
100 Hebei after 2040 (Li et al., 2016).

101  
102 The focus here is in the differences in apparent temperature and PM<sub>2.5</sub> that may arise  
103 from solar geoengineering (that is reduction in incoming short-wave radiation to offset  
104 longwave absorption by greenhouse gases) via stratospheric aerosol intervention (SAI),  
105 and pure greenhouse gas climates. We use all four climate models that have provided  
106 sufficient data from the G4 scenario described by the Geoengineering Model  
107 Intercomparison Project (GeoMIP). G4 specifies sulfates as the aerosol, and greenhouse  
108 gas emissions from the RCP4.5 scenario (Kravitz et al., 2011). The impacts of G4 on  
109 surface temperature and precipitation have been discussed at regional scales (Yu et al.,  
110 2015) and both are lowered relative to RCP4.5. Some studies have focused on regional  
111 impact of SAI on apparent or wet bulb temperatures: in Europe, (Jones et al., 2018);  
112 East Asia (Kim et al., 2020); and the Maritime Continent (Kuswanto et al., 2021). But  
113 none of these studies have considered apparent temperature at scales appropriate for  
114 rapidly urbanizing regions such as on the North China Plain. The only study to date on  
115 SAI impacts on PM<sub>2.5</sub> pollution was a coarse resolution (4°×5°) global scale model with  
116 sophisticated chemistry (Eastham et al., 2018). They simulated aerosol rainout from the  
117 stratosphere to ground level, leading to an eventual increase in ground level PM<sub>2.5</sub>.  
118 Eastham et al. (2018) concluded that SAI changes in tropospheric and stratospheric  
119 ozone dominated PM<sub>2.5</sub> impacts on global mortality. However, this study included only  
120 a first-order estimate of temperature and precipitation change on PM<sub>2.5</sub> concentration  
121 under geoengineering, and also did not consider the situation in a highly polluted urban  
122 environment such as included in our domain, and which is typical of much of the  
123 developing world.

124  
125 The greater Beijing megalopolis lies in complex terrain, surrounded by hills and

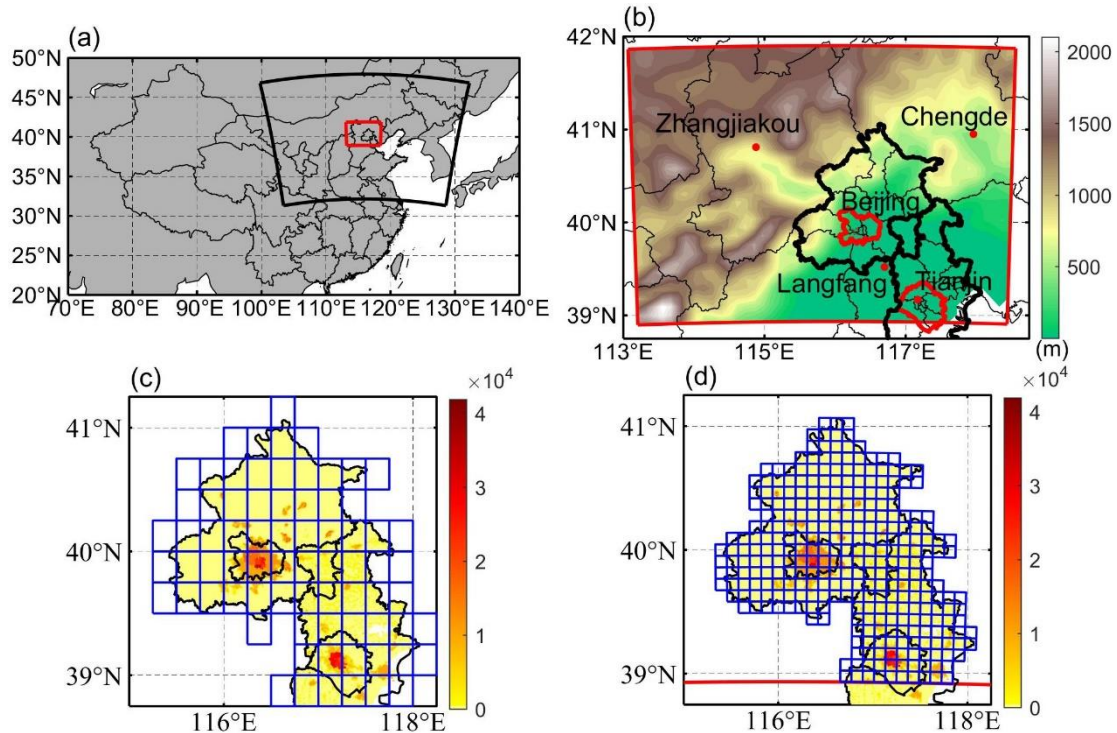
126 mountains on three sides, and a flat plain to the southeast coast (Fig. 1). Over the period  
127 1971-2014, apparent temperature rose at a rate of  $0.42^{\circ}\text{C}/10$  years over Beijing-Tianjin-  
128 Hebei region, with urbanization having an effect of  $0.12^{\circ}\text{C}/10$  years (Luo and Lau,  
129 2021). By the end of 2019, the permanent resident population in Beijing exceeded 21  
130 million. Tianjin, 100 km from Beijing, is the fourth largest city in China with a  
131 population of about 15 million, and Langfang (population 4 million) is about 50 km  
132 from Beijing. Thus, the region contains a comparable urbanized population as the  
133 northeast US megalopolis. Since its climate is characterized by hot and moist summer  
134 monsoon conditions, the population is at an enhanced risk as urban heat island effects  
135 lead to city temperatures warming faster than their rural counterparts.

136

137 There are large uncertainties in projecting  $\text{PM}_{2.5}$  concentration in the future due to both  
138 climate and industrial policies. Statistical methods are much faster than atmospheric  
139 chemistry models (Mishra et al., 2015), and different scenarios are easy to implement.  
140 We use a Multiple Linear Regression (MLR) model to establish the links between  $\text{PM}_{2.5}$   
141 concentration, meteorology and emissions (Upadhyay et al., 2018; Tong et al., 2018).  
142 We project and compare the differences of  $\text{PM}_{2.5}$  concentration under G4 and RCP4.5  
143 scenarios, and between different  $\text{PM}_{2.5}$  emission scenarios. Accurate meteorological  
144 data are crucial in simulating future apparent temperatures and  $\text{PM}_{2.5}$  because all ESM  
145 suffer from bias, and this problem is especially egregious at small scales. A companion  
146 paper (Wang et al., 2022) looked at differences between downscaling methods with the  
147 same 4 Earth System Models (ESM), domain and scenarios as we use here.

148

149 In this paper, we use the downscaled data to explore the effect of SAI on apparent  
150 temperature and  $\text{PM}_{2.5}$  over the greater Beijing megalopolis. The paper is organized as  
151 follows. The data and methods of calculating AP, AP thresholds, the  $\text{PM}_{2.5}$  MLR model  
152 and its validation are briefly described in Section 2. The results from present day  
153 simulation and future projections on apparent temperature and  $\text{PM}_{2.5}$  are given in  
154 Section 3, along with their associated impact analyses. In Section 4 we discuss and  
155 interpret the findings, and finally we conclude with a summary of the main implications  
156 of the geoengineering impacts on these two important human health indices in Section  
157 5.



158 **Figure 1.** **a**, The 10 km WRF domain (red box) nested inside a 30 km resolution WRF domain (large  
 159 black sector). **b**, The inner domain topography and major conurbations (red dots), with the urban areas  
 160 of Beijing and Tianjin enclosed in red curves. Panels **c** and **d** show the population density (persons per  
 161 km<sup>2</sup>) of Beijing and Tianjin provinces (defined by black borders) in 2010 and the grid cells within the  
 162 Beijing-Tianjin province (blue boxes) when downscaled by ISIMIP (**c**) and WRF (**d**).  
 163

## 164 2. Data and Methods

### 165 2.1 Scenarios, ESM, downscaling methods and bias correction

166 The scenarios, ESM, downscaling methods and bias correction methods we use here  
 167 are as described in detail by Wang et al., (2022), and we just summarize the method  
 168 briefly here. We use three different scenarios: RCP4.5 and RCP8.5 (Riahi et al., 2011)  
 169 and the GeoMIP G4 scenario which span a useful range of climate scenarios: RCP4.5  
 170 is similar (Vandyck et al., 2016) to the expected trajectory of emissions under the 2015  
 171 Paris Climate Accord agreed Nationally Determined Contributions (NDCs); RCP8.5  
 172 represents a formerly business-as-usual, no climate mitigation policies, large signal to  
 173 noise ratio scenario; G4 represents a similar radiative forcing as produced by the 1991  
 174 Mount Pinatubo volcanic eruption repeating every 4 years.

175  
 176 Climate simulations are performed by 4 ESM: BNU-ESM (Ji et al., 2014), HadGEM2-  
 177 ES (Collins et al., 2011), MIROC-ESM (Watanabe et al., 2011) and MIROC-ESM-  
 178 CHEM (Watanabe et al., 2011). We compare dynamical and statistical downscaling  
 179 methods to convert the ESM data to scales more suited to capturing differences between  
 180 contrasting rural and urban environments. To validate the downscaled AP from model  
 181 results, we use the daily temperature, humidity and wind speed during 2008-2017 from  
 182 the gridded observational dataset CN05.1 with the resolution of  $0.25^\circ \times 0.25^\circ$  based on

183 the observational data from more than 2400 surface meteorological stations in China,  
184 which are interpolated using the “anomaly approach” (Wu and Gao, 2013). This dataset  
185 is widely used, and has good performance relative to other reanalysis datasets over  
186 China (Zhou et al., 2016; Yang et al., 2019; Yang et al., 2023; Yang and Tang, 2023).  
187 Dynamical downscaling for the 4 ESM datasets was done with WRFv.3.9.1 with a  
188 parameter set used for urban China studies (Wang et al., 2012) in two nested domains  
189 at 30 and 10 km resolution over 2 time slices (2008-2017 and 2060-2069). We corrected  
190 the biases in WRF output using the quantile delta mapping method (QDM; Wilcke et  
191 al., 2013) with ERA5 (Hersbach et al., 2018) to preserve the mean probability density  
192 function of the output over the domain without degrading the WRF spatial pattern. All  
193 WRF results presented are after QDM bias correction. Statistical downscaling was done  
194 with the trend-preserving statistical bias-correction Inter-Sectoral Impact Model  
195 Intercomparison Project (ISIMIP) method (Hempel et al., 2013) for the raw ESM output,  
196 producing output matching the mean ERA5 observational data in the reference  
197 historical period with the same spatial resolution, while allowing the individual ESM  
198 trends in each variable to be preserved.

199

## 200 **2.2 PM<sub>2.5</sub> concentration and emission data**

201 In China there were few PM<sub>2.5</sub> monitoring stations before 2013 (Xue et al., 2021).  
202 However, aerosol optical depths produced by the Moderate Resolution Imaging  
203 Spectroradiometer (MODIS) have been used to build a daily PM<sub>2.5</sub> concentration  
204 dataset (ChinaHighPM2.5) at 1 km resolution from 2000 to 2018 (Wei et al., 2020). We  
205 use monthly PM<sub>2.5</sub> concentration data during 2008-2015 from ChinaHighPM2.5 to train  
206 the MLR model, and the data during 2016-2017 to validate it. Figure S1 shows annual  
207 PM<sub>2.5</sub> concentration over Beijing areas during 2008 (a) and 2017 (b).

208

209 Recent gridded monthly PM<sub>2.5</sub> emission data were derived from the Hemispheric  
210 Transport of Air Pollution (HTAP\_V3) with a resolution of 0.1°×0.1° during 2008-2017,  
211 which is a widely used anthropogenic emission dataset (Janssens-Maenhout et al.,  
212 2015). PM<sub>2.5</sub> emissions over Beijing areas during 2008 (c) and 2017 (d) are shown in  
213 Fig. S1.

214

215 Future gridded monthly PM<sub>2.5</sub> emissions to 2050 are available in the ECLIPSE V6b  
216 database (Stohl et al., 2015), generated by the GAINS (Greenhouse gas Air pollution  
217 Interactions and Synergies) model (Klimont et al., 2017). The ECLIPSE V6b baseline  
218 emission scenario assumes that future anthropogenic emissions are consistent with  
219 those under current environmental policies, hence it is the “worst” scenario without  
220 considering any mitigation measures (Li et al., 2018; Nguyen et al., 2020). Projected  
221 emissions are shown in Fig S2, with emissions plateauing at ~40 kt/year after 2030, so  
222 we assume 2060s levels are similar. These ECLIPSE projections are significantly larger  
223 than present day estimates from HTAP\_V3. We therefore estimate 2060s emissions as  
224 the recent gridded monthly PM<sub>2.5</sub> emissions from HTAP\_V3 scaled by the ratios of  
225 2050 ECLIPSE emission to average annual emissions between 2010 and 2015. Before

226 processing data, PM<sub>2.5</sub> concentration is bilinearly interpolated to the WRF and ISIMIP  
227 grids, while PM<sub>2.5</sub> emissions are conservatively interpolated to the target grids.  
228

## 229 **2.3 Apparent temperature**

230 We used a widely used empirical formula to calculate the apparent temperature under  
231 shade (Steadman 1984), that combines various meteorological fields, which also has  
232 been widely used to study heat waves, heat stress and temperature-related mortality  
233 (Perkins and Alexander, 2013; Lyon and Barnston, 2017; Lee and Sheridan, 2018; Zhu  
234 et al., 2021):

$$235 \quad AP = -2.7 + 1.04 \times T + 2 \times P - 0.65 \times W \quad (1)$$

236 where  $AP$  is the apparent temperature (°C) under shade meaning that radiation is not  
237 considered;  $T$  is the 2 m temperature (°C),  $W$  is the wind speed at 10 m above the ground  
238 (m/s), and  $P$  is the vapor pressure (kPa) calculated by

$$239 \quad P = P_s \times RH \quad (2)$$

240 where  $P_s$  is the saturation vapor pressure (kPa), and  $RH$  is the relative humidity (%).  
241  $P_s$  is calculated using the Tetens empirical formula (Murray, 1966):

$$242 \quad P_s = \begin{cases} 0.61078 \times e^{\left(\frac{17.2693882 \times T}{T+237.3}\right)}, & T \geq 0 \\ 0.61078 \times e^{\left(\frac{21.8745584 \times (T-3)}{T+265.5}\right)}, & T < 0 \end{cases} \quad (3)$$

243 To assess the potential risks of heat-related exposure from apparent temperature, we  
244 also count the number of days with  $AP > 32^\circ\text{C}$  (NdAP\_32) in the Beijing-Tianjin  
245 province (Table S1). This threshold does not lead to extreme risk and death, instead it  
246 is classified as requiring “extreme caution” by the US National Weather Service  
247 (National Weather Service Weather Forecast Office,  
248 <https://www.weather.gov/ama/heatindex>), but carries risks of heatstroke, cramps and  
249 exhaustion. A threshold of  $39^\circ\text{C}$  is classed as “dangerous” and risks heatstroke. While  
250 hotter AP thresholds would give a more direct estimate of health risks, the statistics of  
251 these presently rare events mean that detecting differences between scenarios is less  
252 reliable than using the cooler NdAP\_32 threshold simply because the likelihood of rare  
253 events are more difficult to accurately quantify than more common events that are  
254 sampled more frequently. There is evidence that in some distributions, the likelihood  
255 of extremes will increase more rapidly than central parts of a probability distribution,  
256 for example large Atlantic hurricanes increasing faster than smaller ones (Grinsted et  
257 al., 2013). But the conservative assumption is that similar differences between scenarios  
258 would apply for higher thresholds as lower ones.

## 259 **2.4 Population Data Set**

260 Since health impacts scale with the number of people affected, we calculate the  
261 NdAP\_32 weighted by population (Fig. 1c and 1d). We employ gridded population data  
262 (Fu et al., 2014; <https://doi.org/10.3974/geodb.2014.01.06.V1>) with a spatial resolution  
263 of  $1 \times 1$  km collected in 2010. The population density distribution in Beijing and Tianjin  
264 provinces with the ISIMIP and WRF grid cells contained are shown in the Fig. 1c and  
265 1d.

266

## 267 **2.5 MLR model calibration**

268 Many meteorological factors, such as temperature (You et al., 2017), precipitation (Guo  
269 et al., 2016), wind speed (Yin et al., 2017), radiation (Chen et al., 2017), planetary  
270 boundary layer height (Zheng et al., 2017) etc., can affect the  $PM_{2.5}$  concentration. Their  
271 relative importance differs regionally. But here we consider only differences that are  
272 produced by the three scenarios, so for example we do not include precipitation in our  
273 analysis because none of the ESM simulate significant changes in our domain (Table  
274 S2). Previous studies have shown that wind and humidity are the dominant  
275 meteorological variables for  $PM_{2.5}$  concentration in region we study (Chen et al., 2020),  
276 while changes in temperature and winds obviously impact local concentrations. Hence,  
277 we generate an MLR model between  $PM_{2.5}$  and temperature (T), relative humidity (H),  
278 zonal wind (U), meridional wind (V) and  $PM_{2.5}$  emissions (E) at every grid cell as  
279 follows:

280

$$281 \quad PM_{2.5} = \sum a_i X_i + b \quad (4)$$

282 Where  $X_{i(i=1,2,3,4,5)}$  are the five factors,  $a_i$  are the regression coefficients of the  $X_i$   
283 with  $PM_{2.5}$ , and  $b$  is the intercept, which is a constant. We assume that all factors  
284 should be included in the regression. All the meteorological variables are from the  
285 statistical and dynamical downscaling and bias corrected results during 2008-2017,  
286 with the first 8 years used for training model and the second 2 years used for validating  
287 model. We train the MLR for the 4 ESMs under statistical and dynamical downscaling  
288 in each grid cell separately, thus accounting spatial differences in the weighting of the  
289  $X_i$  across the domain. Meteorological variables under G4, RCP4.5 and RCP8.5 during  
290 2060-2069 are used for projection.

291

292 Here, we use  $PM_{2.5}$  concentration including both primary and secondary  $PM_{2.5}$  as the  
293 dependent variable and primary  $PM_{2.5}$  emission and meteorological factors as  
294 independent variables in the MLR. Future  $PM_{2.5}$  emissions will change in ways that are  
295 rather speculative as they depend on technological innovation and policies that are  
296 inherently unpredictable. The MLR assumes that the past emissions mix and secondary  
297 aerosols remain unchanged in the future, but meteorological factors will also indirectly  
298 impact secondary  $PM_{2.5}$  to some extent.

299

300 The contributions of meteorology and  $PM_{2.5}$  emissions on future concentrations are  
301 examined by using recent  $PM_{2.5}$  emissions (baseline) and future  $PM_{2.5}$  emissions  
302 (mitigation), and the downscaled climate scenarios. Modeled  $PM_{2.5}$  concentration using  
303 recent meteorology and  $PM_{2.5}$  emissions during 2008-2017 (2010s) is considered as our  
304 reference.

305

306 Collinearity of variables is inevitable in our domain. The domination of the seasonal  
307 winter and summer monsoonal weather patterns mean that temperatures, precipitation

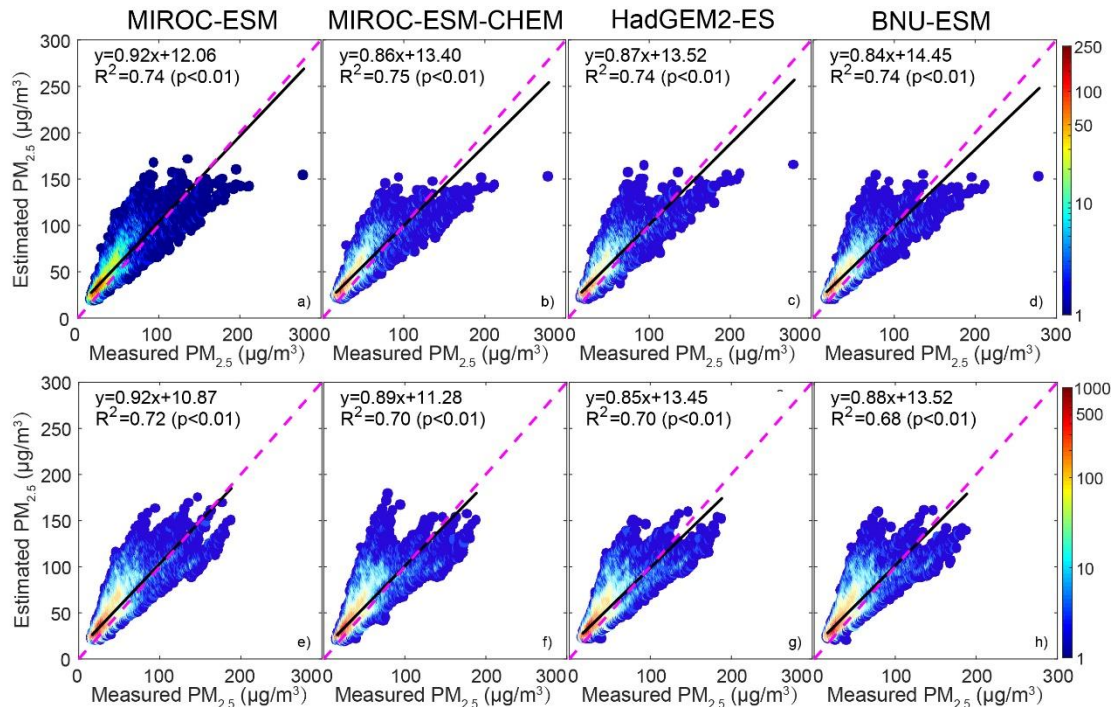


308 and wind direction are all highly seasonal and correlated. In winter, precipitation is  
 309 minimal and northerly winds predominate, in summer the opposite is true. These three  
 310 meteorological fields are important and also important for emissions, since sources are  
 311 essentially absent from the north, while temperature and humidity dominate aerosol  
 312 microphysics.

313

314 We use the variance inflation factor (VIF) to test if there is excessive collinearity in our  
 315 MLR models. Generally, if VIF value is greater than 10, there is collinearity problem  
 316 between variables. Figure S3 shows that there are indeed collinearity problems in some  
 317 areas, but not in Beijing-Tianjin province, so there is no impact on the results for the  
 318 urban areas. We explored the impact of collinearity on the results in high VIF grid cells  
 319 by removing factors with VIF greater than 10 and the full variables model (Fig. S4 and  
 320 Fig. S5). Using ISIMIP downscaling, we only removed the temperature, while we  
 321 removed the temperature and U-wind in the WRF method. PM<sub>2.5</sub> concentrations  
 322 increased by ~1 μg/m<sup>2</sup> in all ESMS under G4 with the “baseline” scenario (Fig. S4), in  
 323 contrast, PM<sub>2.5</sub> concentrations decreased by 5-15 μg/m<sup>2</sup> with the “mitigation” scenario  
 324 (Fig. S5) after dealing the collinearity problem. This means that PM<sub>2.5</sub> concentration  
 325 has more sensitivity to the PM<sub>2.5</sub> emission after accounting for collinearity. Although  
 326 the absolute PM<sub>2.5</sub> concentrations are different accounting for collinearity, there are no  
 327 significant differences in the changes of PM<sub>2.5</sub> concentration between G4 and the  
 328 2010s/RCP4.5/RCP8.5 in Beijing-Tianjin province.

## 329 2.6 MLR model validation



330

331 **Figure 2.** Scattergrams of PM<sub>2.5</sub> concentration derived by MODIS and estimated by MLR during  
 332 validation period (2016-2017). Top figures (a-d) are the ISIMIP statistical downscaling results, and  
 333 bottom figures (e-h) are the WRF dynamical downscaling results. R<sup>2</sup> means the variance explained

334 by the MLR, and color bar denotes the density of datapoints at integer intervals.

335

336 Figure 2 shows the scattergram of PM<sub>2.5</sub> concentration between ChinaHighPM2.5  
337 dataset and MLR model during validation period based on ISIMIP and WRF results.  
338 Observations and MLR models have Pearson's correlations coefficients around 0.86 for  
339 ISIMIP results during the validation period, and the coefficient of determination of  
340 MLRs are 0.74-0.75 (Fig. 2a-d). WRF Pearson's correlations are slightly lower, 0.82-  
341 0.85, and explained variance ranges from 0.68-0.72 (Fig. 2e-h). These results are  
342 similar as found by Jin et al. (2022). We also compare the spatial patterns of observed  
343 and modeled PM<sub>2.5</sub> in Fig. S6. Both ISIMIP and WRF results can simulate the  
344 distribution characteristics of high concentration of PM<sub>2.5</sub> in the southeast and low  
345 concentration in the northwest.

346

347 We also tested the accuracy of our MLR model projection against simulations (Li et al.,  
348 2023) with the Community Multiscale Air Quality (CMAQ) model developed by the  
349 United States Environmental Protection Agency and which can simulate particulate  
350 matter on local scales (Foley et al., 2010; Yang et al., 2019) when coupled to WRF. We  
351 used the same meteorological forcing as Li with the "EIT1" PM<sub>2.5</sub> emissions scenario  
352 in 2050 under RCP4.5 (Fig.S7). The spatial patterns are well correlated in all seasons  
353 (0.68-0.73), but PM<sub>2.5</sub> concentrations are about twice as high in our MLR model as  
354 from Li et al., (2023). PM<sub>2.5</sub> concentrations from our regression model are also higher  
355 than the referenced data during 2008-2017. While the difference in absolute PM<sub>2.5</sub>  
356 concentrations are significant, we mainly consider differences of PM<sub>2.5</sub> concentration  
357 between G4 and RCP4.5/RCP8.5 in our study which we cannot compare these  
358 anomalies with the single RCP4.5 scenario simulated by Li et al. (2023). We do  
359 compare the spatial pattern of differences in PM<sub>2.5</sub> concentration between "base" and  
360 "EIT1" under RCP4.5. Because of the small slope coefficient of PM<sub>2.5</sub> emission in our  
361 MLR, we do not capture the large reduction of PM<sub>2.5</sub> concentration in the Beijing city  
362 center seen by Li et al. (2023), (Fig. S8).

363

## 364 **2.7 Relative risks of mortality related to PM<sub>2.5</sub>**

365 We estimate the effects of PM<sub>2.5</sub> on mortality by considering changes in the relative risk  
366 (RR) of mortality related to PM<sub>2.5</sub>. We lack data on mortality rates in the study domain  
367 without which we cannot estimate numbers of fatalities, just the average population-  
368 weighted RR. Burnett et al. (2014) established the integrated exposure-response  
369 functions we use. The RR is non-linear in concentration, that is an initially low PM<sub>2.5</sub>  
370 region will suffer higher mortality and RR than an initially high PM<sub>2.5</sub> region if PM<sub>2.5</sub>  
371 is increased by the same amount. Ran et al. (2023) provide RR values for PM<sub>2.5</sub>  
372 concentrations up to 200 µg/m<sup>3</sup> that includes the 5 main major disease endpoints  
373 (Global Burden of Disease Collaborative Network, 2013) of PM<sub>2.5</sub> related mortality:  
374 chronic obstructive pulmonary disease, ischemic heart disease, lung cancer, lung  
375 respiratory infection and stroke. We calculate the average population-weighted relative  
376 risks based on the gridded population dataset (Section 2.4) and PM<sub>2.5</sub> concentration in

377 the Beijing-Tianjin province defined in the Fig. 1c-1d, following Ran et al. (2023):

378 
$$RR_{pop,k} = \frac{\sum_{g=1}^G POP_g \times RR_k(C_g)}{\sum_{g=1}^G POP_g} \quad (5)$$

379  $RR_{pop,k}$  is the average population-weighted relative risk of disease  $k$  ( $k=1-5$ ),  $POP_g$  is  
380 the population of grid  $g$ , and  $RR_k(C_g)$  is the relative risk of disease  $k$  when  $PM_{2.5}$   
381 concentration is  $C_g$  in the grid of  $g$ .

382

## 383 **2.8 Determination of contributions to change in AP and $PM_{2.5}$**

384 Equation (1) describes how AP is calculated, and this can be broken down into how  
385 much equivalent temperature is produced by each term (Fig. 3), with 2008-2017 as the  
386 baseline interval for season-by-season contributors to AP. Across scenario seasonal  
387 differences in contributors are then calculated as follows. We use an MLR approach,  
388 since this minimizes the square differences from the mean across the dataset, with the  
389 attendant assumption of independence between the data. Alternatives may also be  
390 considered that e.g. minimize the impact of outliers by considering the magnitude of  
391 the differences, but we prefer to keep the attractive properties of a least squares  
392 approach. The dependent variable in the MLR is the change in AP ( $\Delta AP$ ) and the  
393 independent variables are changes in each factor for each future scenario,

394 
$$\Delta AP = \sum \alpha_i X_i + \beta \quad (6)$$

395 where  $X_{i(i=1,2,3)}$  are the daily changes of the three meteorological factors between two  
396 scenarios: 2 m temperature ( $\Delta T$ ), 2 m relative humidity ( $\Delta RH$ ) and 10 m wind speed  
397 ( $\Delta W$ ),  $\alpha_i$  are the regression coefficients of the  $X_i$  with  $\Delta AP$ , and  $\beta$  is the intercept,  
398 which is a constant. We assume that all three meteorological factors should be included  
399 in the regression and we estimate the contributions of each factor to changes of  $AP$  as:

400 
$$K_i = \frac{\alpha_i \bar{X}_i}{\sum \alpha_i \bar{X}_i} \quad (7)$$

401 where  $K_{i(i=1,2,3)}$  is the contributions (in units of temperature) from each factor to the  
402 changes of the AP, and  $\bar{X}_i$  are the mean differences in temperature equivalent due to  
403 each factor between two scenarios.

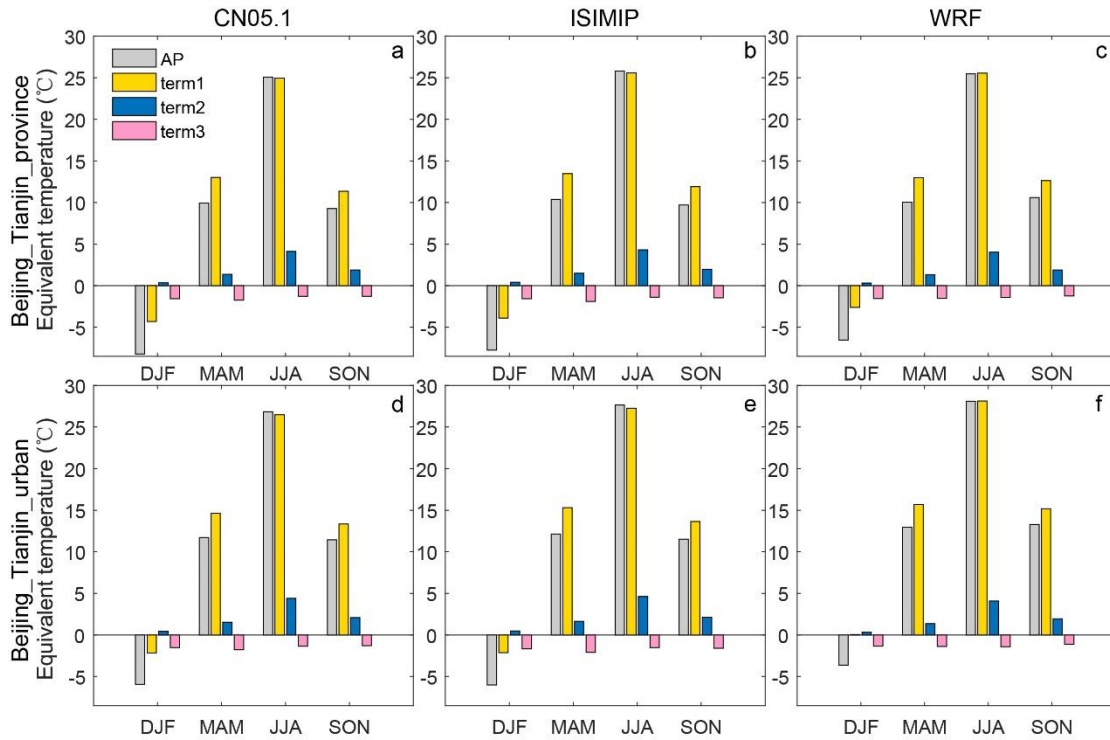
404

405 The contribution of changes in each factor in changes of  $PM_{2.5}$  is simpler since we  
406 assume that the relationship between each factor and  $PM_{2.5}$  is linear, and so its  
407 contribution is the ratio of product of the regression coefficient and the change of each  
408 factor to the change of  $PM_{2.5}$ .

409

## 410 **3. Results**

### 411 **3.1 Recent apparent temperatures**



412

413

**Figure 3.** Seasonal averaged AP and equivalent temperature of each term in equation 1 for Beijing-Tianjin province (a-c) and Beijing-Tianjin urban areas (d-f) during 2008-2017 from CN05.1 (a, d), 4-model ensemble mean after ISIMIP (b, e) and ensemble mean after WRF (c, f). Term 1 is 1.04T, term 2 is 2P and term 3 is -0.65W.

417

418

419

420

421

422

423

424

425

426

427

428

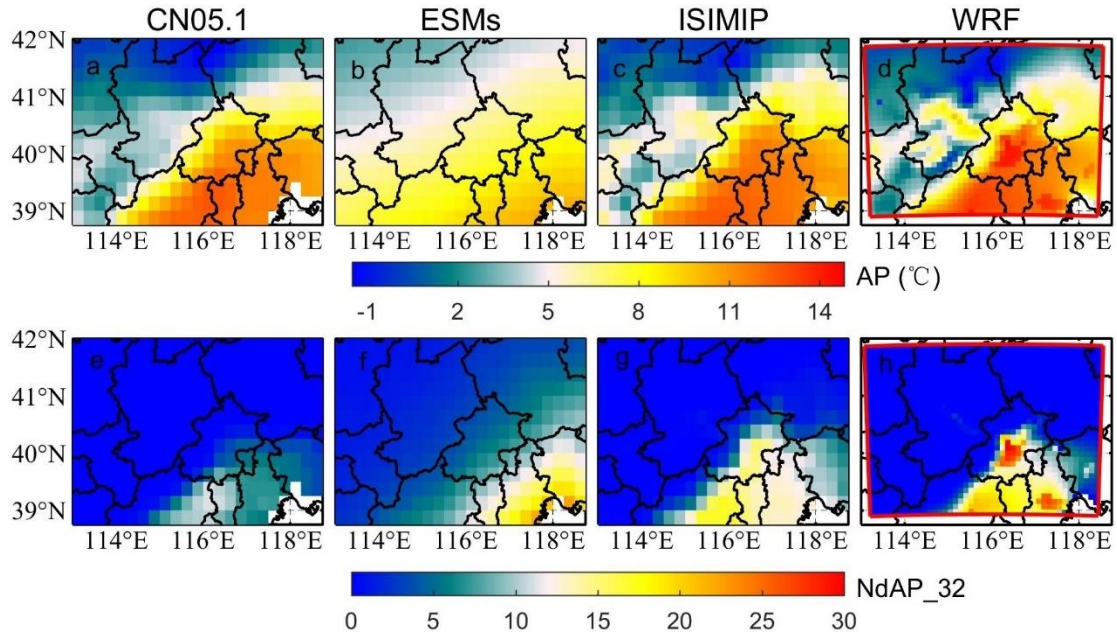
429

430

431

432

Figure 3 shows the seasonal averaged AP and equivalent temperatures caused by temperature, relative humidity and wind speed in Beijing-Tianjin province and Beijing-Tianjin urban areas during 2008-2017. According to the CN05.1 results (Fig. 3a, 3d), AP and the separate 3 terms show similar seasonal patterns over the whole province and just the urban areas. Vapor pressure is higher in summer and wind speed is higher in spring. AP is lower than 2 m temperature in all seasons except summer, and especially lower in winter. AP, temperature, vapor pressure and wind speed are all higher in urban areas than in the surrounding rural region in any season. The ISIMIP results (Fig. 3b, 3e), by design, perfectly reproduce the CN05.1 seasonal characteristics of AP, temperature, vapor pressure and wind speed. WRF shows a similar pattern with that from CN05.1, but for the Beijing-Tianjin province, WRF overestimates both 2 m temperature and AP in winter by 2.1°C and by 1.7°C respectively relative to CN05.1 (Fig. 3c). In the Beijing-Tianjin urban areas, WRF overestimates the temperature and AP relative to CN05.1 in all seasons, especially in winter (Fig. 3f).



433

434 **Figure 4.** Top row: the spatial distribution of mean apparent temperature from CN05.1 (a), raw ESMs  
 435 ensemble mean after bilinear interpolation (b), 4-model ensemble mean after ISIMIP (c) and ensemble  
 436 mean after WRF (d) during 2008-2017. Bottom row: the spatial distribution of annual mean number of  
 437 days with AP > 32°C from CN05.1 (e), ESMs (f), ISIMIP (e) and WRF (f) during 2008-2017. Fig. S9  
 438 and Fig. S10 show the pattern of AP and NdAP\_32 for the individual ESM.

439 We compare the simulations of mean apparent temperature and NdAP\_32 from both  
 440 WRF dynamical downscaling with QDM and from ISIMIP statistical downscaling  
 441 during 2008-2017 in Fig. 4. Both WRF with QDM and ISIMIP methods produce a  
 442 pattern of apparent temperature which is close to that from CN05.1. While the raw AP  
 443 from ESMs is overestimated in Zhangjiakou high mountains and underestimated in the  
 444 southern plain, and shares a similar pattern with temperature from ESMs (Wang et al.,  
 445 2022). The raw ESM outputs were improved after dynamical and statistical  
 446 downscaling. The average annual AP from ISIMIP (9.6-9.7°C) is 0.5°C higher than that  
 447 from CN05.1 (9.1°C) over the Beijing-Tianjin province for all ESMs (Table 1). While  
 448 WRF produces warmer apparent temperatures in the city centers of Beijing and Tianjin  
 449 and lower ones in the high Zhangjiakou mountains than recorded in the lower resolution  
 450 CN05.1 observations. There are also differences between different models after WRF  
 451 downscaling. For example, apparent temperatures from the two MIROC models  
 452 downscaled by WRF are the warmest. In contrast AP from all 4 ESMs after ISIMIP  
 453 shows very similar patterns (Fig. S9).

454

455 ESMs tend to overestimate the number of days with AP>32°C in southeastern Beijing  
 456 and the whole Tianjin province. Both ISIMIP and WRF appear to overestimate the  
 457 NdAP\_32 in Beijing urban areas and the southerly lowland areas although NdAP\_32 is  
 458 close to zero in the colder rural areas at relatively high altitude for both downscaling  
 459 methods. Some of these differences may be due to the WRF simulations being at finer  
 460 resolution than the 0.25°× 0.25° CN05.1, leading to higher probabilities of high AP in  
 461 urban areas (Fig. 5d). ISIMIP results also show slight overestimations, especially in the

462 tails of the distribution ( $AP > 30^{\circ}\text{C}$ ) for urban areas (Fig. 5c). CN05.1 gives about 5  
 463 NdAP\_32 per year in southern Beijing and Tianjin, but there are nearly 15 NdAP\_32  
 464 from ISIMIP, and over 20 NdAP\_32 per year from WRF downscaling in the Beijing-  
 465 Tianjin urban areas during 2008-2017. NdAP\_32 from WRF and ISIMIP downscaling  
 466 of all ESM is overestimated relative to CN05.1. But there are differences in ESM under  
 467 the two downscalings: with ISIMIP, HadGEM2-ES and BNU-ESM have more  
 468 NdAP\_32 than the two MIROC models, while the reverse occurs with WRF (Fig. S10).  
 469

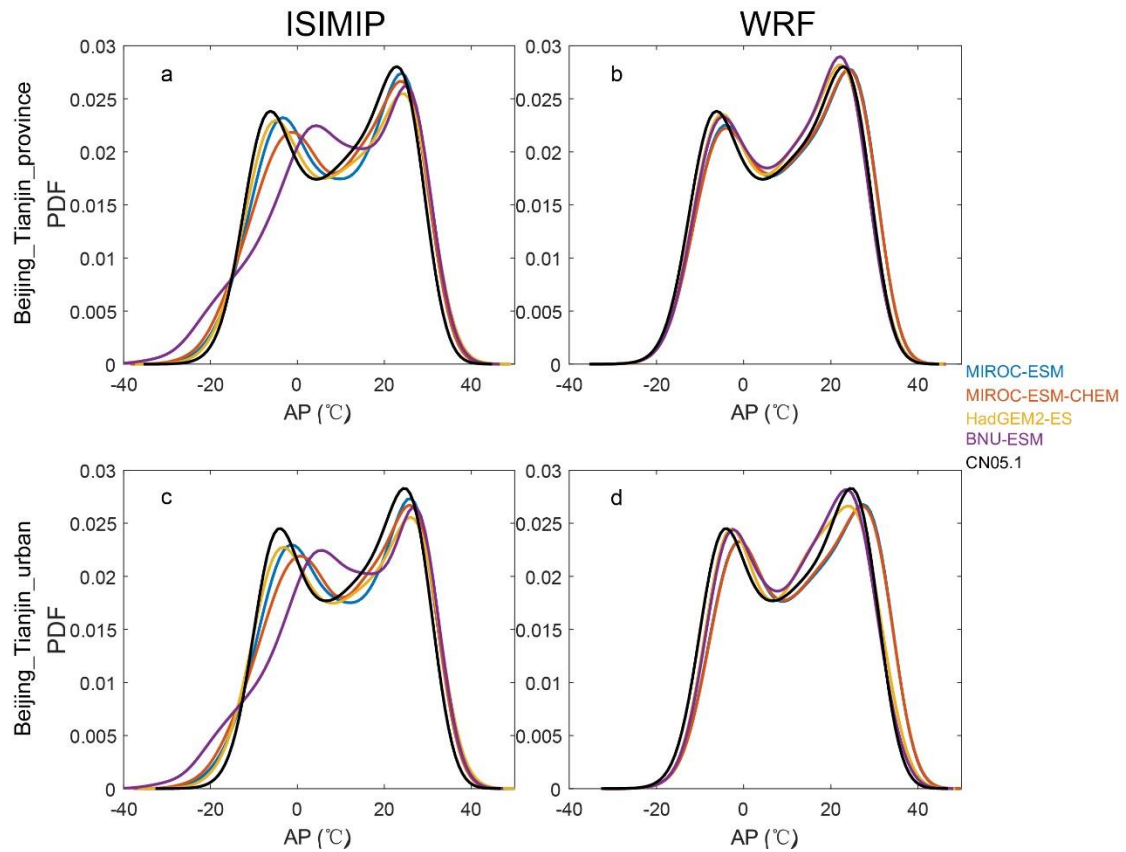
470 **Table 1.** The annual mean apparent temperature and population weighted NdAP\_32 in Beijing-Tianjin  
 471 province and Beijing-Tianjin urban areas (Fig. 1b) from CN05.1, ISIMIP and WRF during 2008-2017.

Data Sources	AP ( $^{\circ}\text{C}$ )				NdAP_32 (day yr $^{-1}$ )	
	Provinces		Urban		Population weighted for province (Fig. 1c, 1d)	
	WRF	ISIMIP	WRF	ISIMIP	WRF	ISIMIP
MIROC-ESM	10.5	9.6	13.6	11.4	22.2	10.1
MIROC-ESM-CHEM	10.5	9.6	13.6	11.4	21.9	11.0
HadGEM2-ES	9.5	9.6	12.0	11.4	12.3	11.1
BNU-ESM	9.4	9.7	11.8	11.5	10.2	12.7
CN05.1	9.1		11.1		2.4	

472 The Taylor diagram of the daily mean apparent temperature in Beijing-Tianjin province  
 473 and Beijing-Tianjin urban areas from 2008-2017 for the 4 ESMs shows that correlation  
 474 coefficients between ESMs and CN05.1 are greater than 0.85 under both downscaling  
 475 methods. Although there are differences between ESMs, the performance of WRF, with  
 476 higher correlation coefficient and smaller SD (standard deviation) and RMSD (root  
 477 mean standard deviation), is usually superior to ISIMIP (Fig. S11). Taking the Beijing-  
 478 Tianjin urban areas as an example (Fig. S11b), under the ISIMIP method, MIROC-  
 479 ESM, MIROC-ESM-CHEM and HadGEM2-ES have the same correlation coefficient  
 480 (0.92) and RMSD ( $5.4^{\circ}\text{C}$ ) with the CN05.1, while BNU-ESM has lower correlation  
 481 coefficient (0.88) and higher RMSD ( $7.0^{\circ}\text{C}$ ). Under WRF simulations, MIROC-ESM  
 482 and MIROC-ESM-CHEM have larger correlation coefficients and smaller RMSD with  
 483 CN05.1 than HadGEM2-ES and BNU-ESM.

484 Figure 5 shows the probability density functions (pdf) of daily AP from the four ESMs  
 485 under ISIMIP and WRF in Beijing-Tianjin province and Beijing-Tianjin urban areas  
 486 during 2008-2017. ISIMIP overestimates the probability of extreme cold AP relative to  
 487 CN05.1 (especially BNU-ESM), although all ESM reproduce the CN05.1 pdf well at  
 488 high AP. WRF can reproduce the CN05.1 distribution of AP better than ISIMIP, but  
 489 high AP is overestimated relative to CN05.1 and the urban areas perform less well than  
 490 the whole Beijing-Tianjin province. In urban areas all ESMs driving WRF tend to  
 491 underestimate the probability of lower AP and to overestimate the probability of higher  
 492 AP, especially the two MIROC models (Fig. 5d). Fig. S12 displays the annual cycle of  
 493 monthly AP, with ISIMIP proving excellent by design, at reproducing the monthly AP.  
 494 While under WRF downscaling AP shows more across model differences, especially  
 495 during summer and with greater spread for the urban areas.



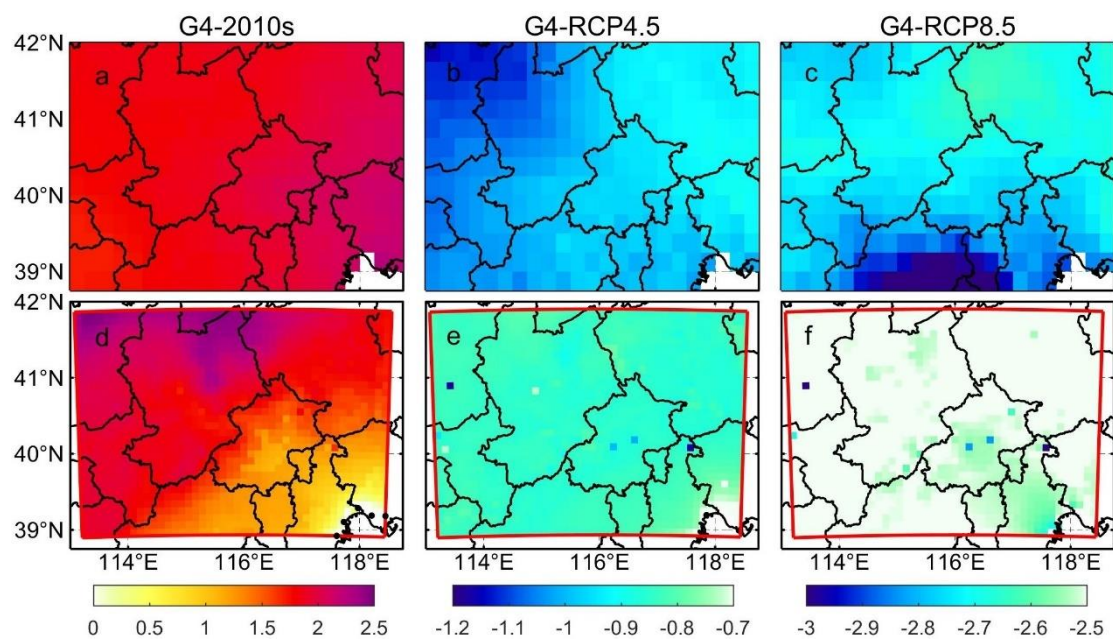


496

497 **Figure 5.** The probability density function (pdf) for daily apparent temperature under ISIMIP (a, c) and  
 498 WRF (b, d) results in Beijing-Tianjin province (a, b) and Beijing-Tianjin urban areas (c, d) during 2008-  
 499 2017.

## 500 3.2 2060s apparent temperatures

### 501 3.2.1 Changes of apparent temperature



502

503 **Figure 6.** Spatial pattern of ensemble mean apparent temperature difference (°C) under different  
 504 scenarios over 2060-2069: G4-2010s (left column), G4-RCP4.5 (middle column) and G4-RCP8.5 (right  
 505 column) based on ISIMIP and WRF methods. 2010s refers to the 2008-2017 period. Stippling indicates  
 506 grid points where differences or changes are not significant at the 5% level according to the Wilcoxon  
 507 signed rank test.

508  
 509 Figure 6 shows the ISIMIP and WRF ensemble mean changes in the annual mean AP  
 510 under G4 during 2060-2069 relative to the past and the two future RCP scenarios.  
 511 ISIMIP-downscaled AP (Fig. 6a-6c) shows significant anomalies ( $p < 0.05$ ), with whole  
 512 domain rises of 2.0 °C in G4-2010s, and falls of 1.0 °C and 2.8 °C in G4-RCP4.5 and  
 513 G4-RCP8.5 respectively. In WRF results, AP under G4 is about 1-2 °C warmer than  
 514 that under 2010s, 0.8 °C and 2.5 °C colder than that under RCP4.5 and RCP8.5 over  
 515 the whole domain. Individual ESM results downscaled by ISIMIP and WRF are in Fig.  
 516 S14 and Fig. S15. For both ISIMIP and WRF downscaling results, the two MIROC  
 517 models show stronger warming than the other two models between G4 and the 2010s.  
 518 WRF-downscaled AP driven by HadGEM2-ES exhibits the strongest cooling, with  
 519 decreases of 1.7 °C between G4 and RCP4.5 and falls of 3.0 °C between G4 and RCP8.5.  
 520 Although different ESMs show different changes in AP between G4 and other scenarios,  
 521 changes in AP are almost the same everywhere for a given ESM in the ISIMIP results  
 522 (Fig. S14). WRF-downscaled AP anomalies driven by two MIROC models are larger  
 523 in the Zhangjiakou mountains and smaller in the Beijing urban areas and Tianjin city  
 524 between G4 and 2010s (Fig. S15). Changes in AP from ISIMIP results, whether across  
 525 whole province or just the urban areas, are statistically identical given scenarios (Table  
 526 2), which is consistent with patterns in figure 6. AP under G4 is 0.8 °C (1.0 °C) and  
 527 2.6 °C (2.8 °C) colder than that under RCP4.5 and RCP8.5 in Beijing-Tianjin urban  
 528 areas from ISIMIP (WRF) results. The warming between G4 and 2010s in urban areas  
 529 is 1.0 °C in WRF results, while that is 2.0 °C in ISIMIP results (Table 2).

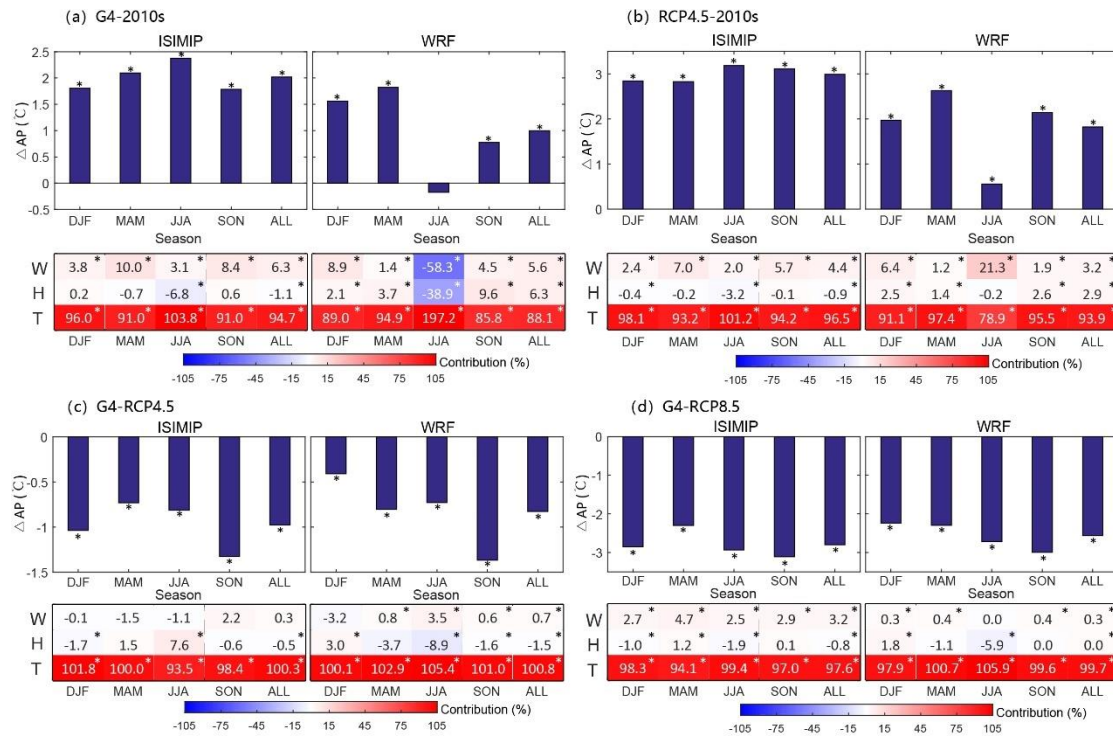
530  
 531 **Table 2.** Difference of apparent temperature between the G4 and other scenarios for the Beijing-Tianjin  
 532 province and Beijing-Tianjin urban areas as defined in Fig. 1b during 2060-2069. Bold indicates the  
 533 differences or changes are significant at the 5% level according to the Wilcoxon signed rank test.  
 534 (Units: °C)

Model	G4-2010s				G4-RCP4.5				G4-RCP8.5			
	WRF		ISIMIP		WRF		ISIMIP		WRF		ISIMIP	
	Urban	Province	Urban	Province	Urban	Province	Urban	Province	Urban	Province	Urban	Province
MIROC-ESM	<b>0.9</b>	<b>1.5</b>	<b>2.2</b>	<b>2.2</b>	<b>-0.5</b>	<b>-0.4</b>	<b>-0.9</b>	<b>-0.9</b>	<b>-2.3</b>	<b>-2.1</b>	<b>-2.8</b>	<b>-2.7</b>
MIROC-ESM-CHEM	<b>0.9</b>	<b>1.5</b>	<b>2.9</b>	<b>2.8</b>	<b>-0.4</b>	<b>-0.4</b>	-0.1	-0.1	<b>-2.0</b>	<b>-2.0</b>	<b>-2.1</b>	<b>-2.1</b>
HadGEM2-ES	<b>1.1</b>	<b>1.0</b>	<b>1.8</b>	<b>1.7</b>	<b>-1.6</b>	<b>-1.6</b>	<b>-1.6</b>	<b>-1.6</b>	<b>-3.1</b>	<b>-3.1</b>	<b>-3.3</b>	<b>-3.3</b>
BNU-ESM	<b>1.2</b>	<b>1.1</b>	<b>1.2</b>	<b>1.3</b>	<b>-0.8</b>	<b>-0.8</b>	<b>-1.3</b>	<b>-1.3</b>	<b>-2.8</b>	<b>-2.7</b>	<b>-2.9</b>	<b>-2.9</b>
Ensemble	<b>1.0</b>	<b>1.3</b>	<b>2.0</b>	<b>2.0</b>	<b>-0.8</b>	<b>-0.8</b>	<b>-1.0</b>	<b>-1.0</b>	<b>-2.6</b>	<b>-2.5</b>	<b>-2.8</b>	<b>-2.8</b>

535

### 536 3.2.2 Contributing factors to changes in AP





537

538 **Figure 7.** The seasonal changes of AP ( $\Delta AP$ ) and the seasonal contribution of climatic factors to  $\Delta AP$   
 539 for Beijing and Tianjin urban areas under ISIMIP and WRF between G4 and 2010s **(a)**, G4 and 2010s  
 540 **(b)**, G4 and RCP4.5 **(c)** and G4 and RCP8.5 **(d)** in the 2060s based on ensemble mean results. Colors  
 541 and numbers in each cell correspond to color bar, and “\*” above the columns and in the cells indicate  
 542 differences are significant at the 5% significant level under the Wilcoxon test.

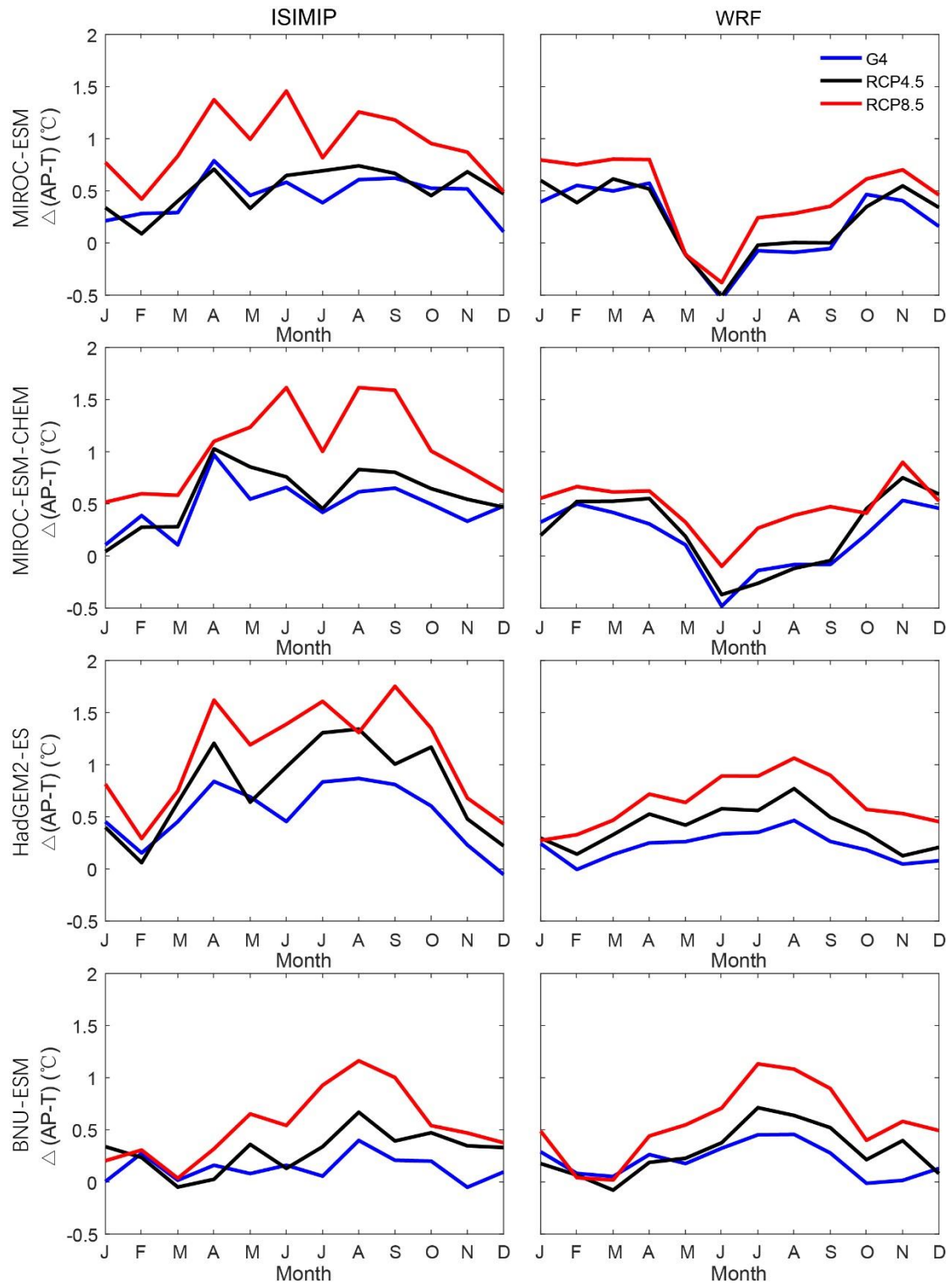
543

544 Figure 7 shows the ISIMIP and WRF ensemble mean changes in the annual mean AP  
 545 anomalies G4 during 2060-2069 relative to the past and the two future RCP scenarios.  
 546 ISIMIP-downscaled AP (Fig. 7a-7c) shows significant anomalies ( $p < 0.05$ ) across the  
 547 whole domain, even for the relatively small differences in G4-RCP4.5.  $\Delta AP$  by WRF  
 548 is lower than that by ISIMIP. Between G4 and 2010s, AP are projected to have increases  
 549 of 1.8 (1.6), 2.1 (1.8), 2.4 (-0.2), 1.8 (0.8) °C from winter to autumn in ISIMIP (WRF)  
 550 results. In ISIMIP results, the contribution of temperature ranges from 91%-104%, and  
 551 the contribution of wind speed ranges from 3%-10% in all seasons, while the  
 552 contribution of humidity is negative or insignificant (Fig. 7a). However, the  
 553 contribution of humidity is positive in WRF results (Fig. 7a). Between RCP4.5 and  
 554 2010s, annual mean AP is projected to increase by 3.0 °C and 1.8 °C in ISIMIP and  
 555 WRF results respectively, which is higher than that between G4 and 2010s. The increase  
 556 of temperature and decrease of wind speed have a significant impact on the annual  
 557 average  $\Delta AP$  contributed 97% (94%) and 4% (3%) in ISIMIP (WRF) results. The  
 558 contributions of changes in humidity are significantly positive under G4 and RCP4.5 in  
 559 WRF results, while it is the opposite in the ISIMIP results (Fig. 7a-7b).

560

561 Relative to RCP4.5 in the 2060s, AP is projected to decrease by 1.0 (0.4), 0.7 (0.8), 0.8  
 562 (0.7), and 1.3 (1.4) °C from winter to autumn under G4 in ISIMIP (WRF) results (Fig.  
 563 7c). In summer, the contribution from changes in temperature and humidity are 94%

564 (105%) and 8% (-9%) in ISIMIP (WRF) results, respectively. There are insignificant  
 565 contributions from wind speed under ISIMIP results, but a significant slight positive  
 566 contribution (0.7%-4%) under WRF results (Fig. 7c). The annual mean AP under G4 is  
 567 2.8 (2.6) °C lower than that under RCP8.5 in ISIMIP (WRF) result. In this case, the  
 568 contribution of changes in wind on  $\Delta AP$  ranges from 3%-5% by ISIMIP, while it is  
 569 close to 0 by WRF. As expected,  $\Delta AP$  is mainly determined by the changes in  
 570 temperature, with contributions usually above 90% between different scenarios.



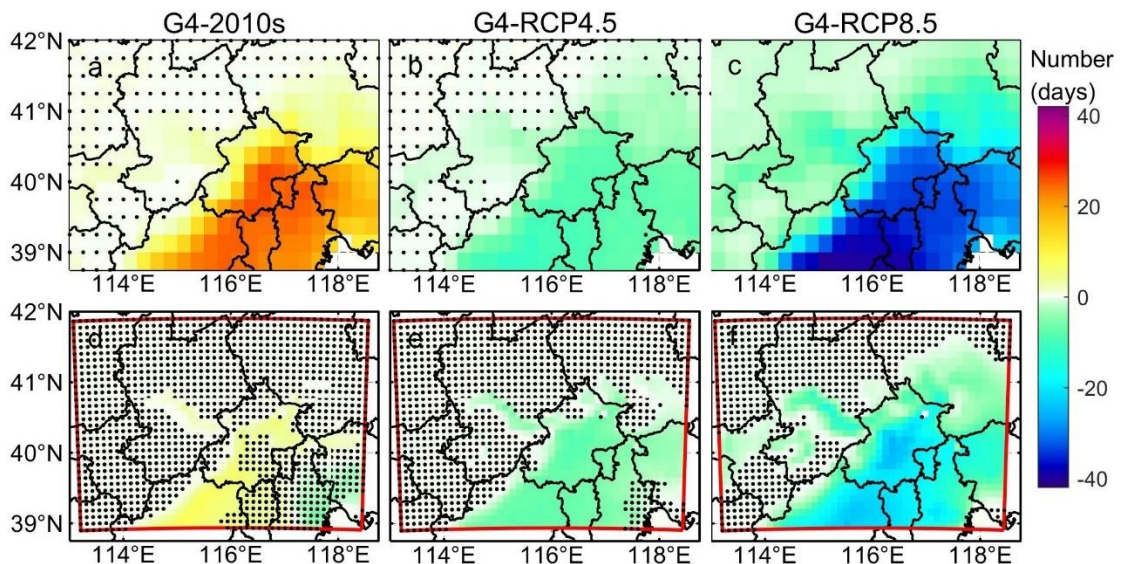
571

572 **Figure 8.** The change of apparent temperature based on air temperature under three scenarios (G4,  
 573 RCP4.5 and RCP8.5) in four ESMs under ISIMIP (left column) and WRF (right column) for urban areas  
 574 relative to the 2010s.

575

576 A useful measure of heat impacts that may be missed if considering only at air  
 577 temperatures is the seasonality of the differences between AP and air temperature  
 578 ( $\Delta(\text{AP-T})$ ; Fig. 8). The four model ensemble annual mean  $\Delta(\text{AP-T})$  under ISIMIP is  
 579 projected to rise by 0.4°C, 0.5°C and 0.9°C under G4, RCP4.5 and RCP8.5, relative to  
 580 the 2010s. Under WRF,  $\Delta(\text{AP-T})$  is much smaller than under ISIMIP but still rising  
 581 faster than air temperatures: by 0.2°C, 0.3°C and 0.5°C under G4, RCP4.5 and RCP8.5  
 582 relative to the 2010s, respectively. In general, the largest anomalies in  $\Delta(\text{AP-T})$  are in  
 583 summer under both WRF and ISMIP downscaling, but the two MIROC models under  
 584 WRF have small or even negative  $\Delta(\text{AP-T})$  in summer with WRF.

### 585 3.2.3 Changes of the number of days with AP>32°C



586

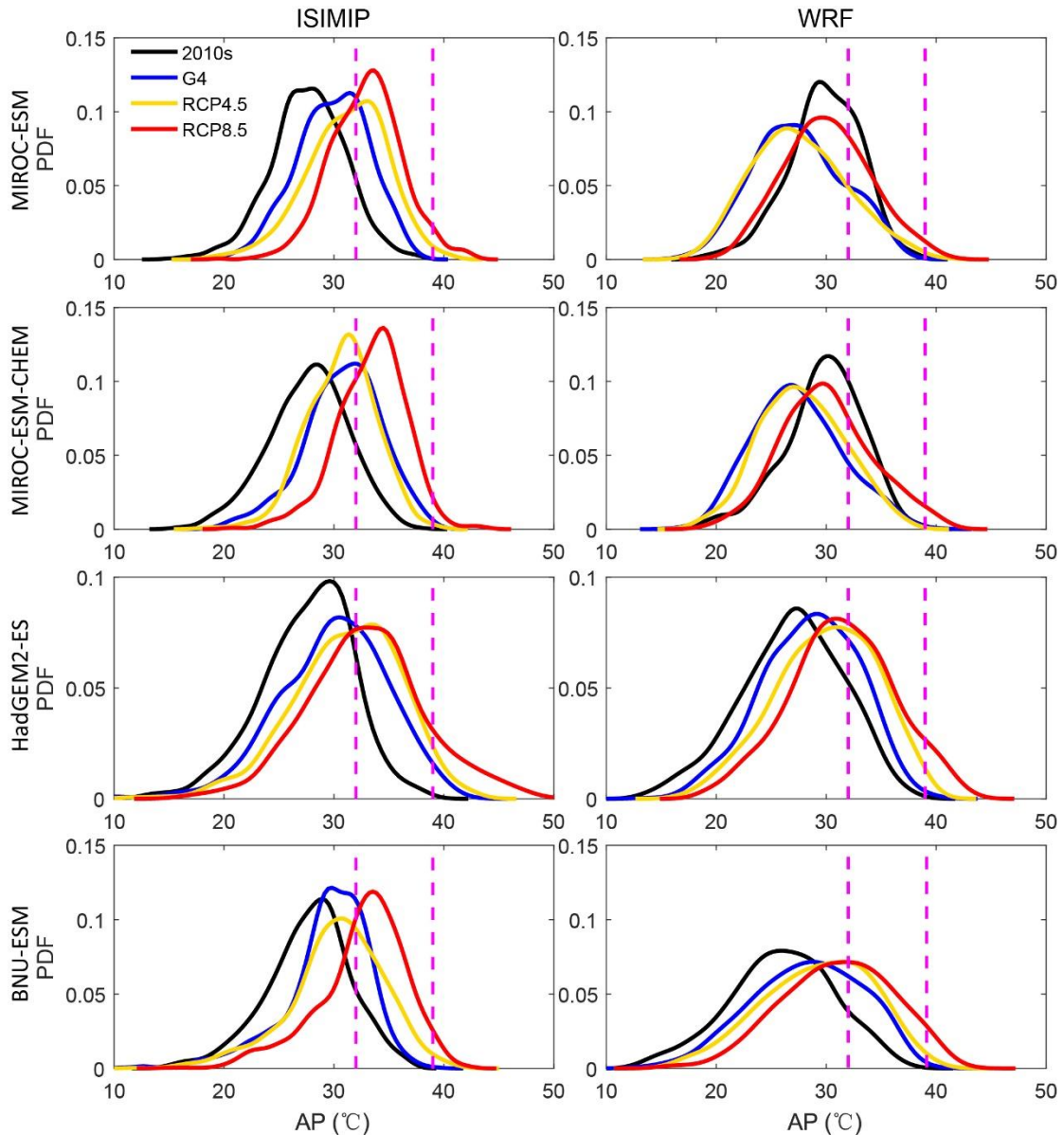
587 **Figure 9.** Ensemble mean differences in annual number of days with AP > 32°C (NdAP\_32) between  
 588 scenarios for 2060-2069: G4-2010s (left column), G4-RCP4.5 (second column) and G4-RCP8.5 (right  
 589 column) based on ISIMIP method and WRF. 2010s means the results simulated during 2008-2017.  
 590 Stippling indicates grid points where differences or changes are not significant at the 5% level according  
 591 to the Wilcoxon signed rank test. Corresponding ISIMIP results for each ESM are in Fig. S16, and WRF  
 592 results in Fig. S17.

593

594 The NdAP\_32 anomalies in Figure 9 show that ISIMIP projects an increase of about 20  
 595 days per year with AP>32 °C for the southeast of Beijing province and 10 days in the  
 596 western areas of Beijing under G4 relative to the 2010s. NdAP\_32 is about 10 days  
 597 fewer under G4 than RCP4.5 with no clear spatial differences. G4 has about 35 fewer  
 598 NdAP\_32 days in the southern part of the domain and 20 fewer days in the western  
 599 domain than the RCP8.5 scenario. In contrast WRF suggests that most areas do not  
 600 show any significant difference between G4 and the 2010s, while the anomalies relative  
 601 to RCP4.5 are similar as ISIMIP, the differences are insignificant over more area than



602 ISIMIP. G4-RCP8.5 anomalies with WRF are smaller than with ISIMIP, and differences  
 603 are not significant in the Zhangjiakou high mountains. The urban areas show larger  
 604 decreases in NdAP\_32 than the more rural areas, even in the low altitude plain.  
 605 Individual ESM show almost no statistically significant differences between G4 and  
 606 RCP4.5 (Fig. S16 and S17), but the differences seen in Fig. 9 are significant because of  
 607 the larger sample size in the significance test. All ESMs with ISIMIP show more  
 608 NdAP\_32 in the urban areas under G4 than the 2010s, while two MIROC models  
 609 driving WRF show fewer NdAP\_32 in Beijing-Tianjin urban areas (Fig. S16, S17).  
 610



611  
 612 **Figure 10.** Probability density distributions of daily apparent temperature (AP) in summer (JJA) over  
 613 Beijing-Tianjin urban areas under recent period (2008-2017), and the 2060s under G4, RCP4.5 and  
 614 RCP8.5 scenarios from ISIMIP and WRF results. The purple dotted lines are at AP of 32°C and 39°C.  
 615

616 The pdf of daily apparent temperature in summer over Beijing-Tianjin urban areas (Fig.  
 617 10) shifts rightwards for G4, RCP4.5 and RCP8.5 during the 2060s relative to the 2010s.

618 Figure 10 shows that by the 2060s, the dangerous threshold of  $AP > 39$  is crossed  
 619 frequently under RCP8.5 with both WRF and ISIMIP downscaling, but for the RCP4.5  
 620 and G4 scenarios these events are much rarer. ISIMIP results tend to show higher  
 621 probability tails (extreme events) than under WRF simulations.

622

623 Population weighted  $NdAP_{32}$  in the 2060s for Beijing-Tianjin province is shown in  
 624 Table 3. ISIMIP downscaling suggests ensemble mean rises in  $NdAP_{32}$  of 22.4 days  
 625 per year under G4 relative to the 2010s, but that G4 has 8.6 and 33.5 days per year  
 626 fewer than RCP4.5 and RCP8.5, respectively.  $NdAP_{32}$  from WRF under G4 is  
 627 reduced by 19.6 days per year relative to RCP8.5, and by 6.3 days relative to RCP4.5  
 628 (Table 3).

629

630 **Table 3.** Difference of population weighted  $NdAP_{32}$  between the G4 and other scenarios for Beijing-  
 631 Tianjin province (Fig. 1c, 1d) during 2060-2069. Bold indicates the changes are significant at the 5%  
 632 level according to the Wilcoxon signed rank test. (Units:  $\text{day y}^{-1}$ ).

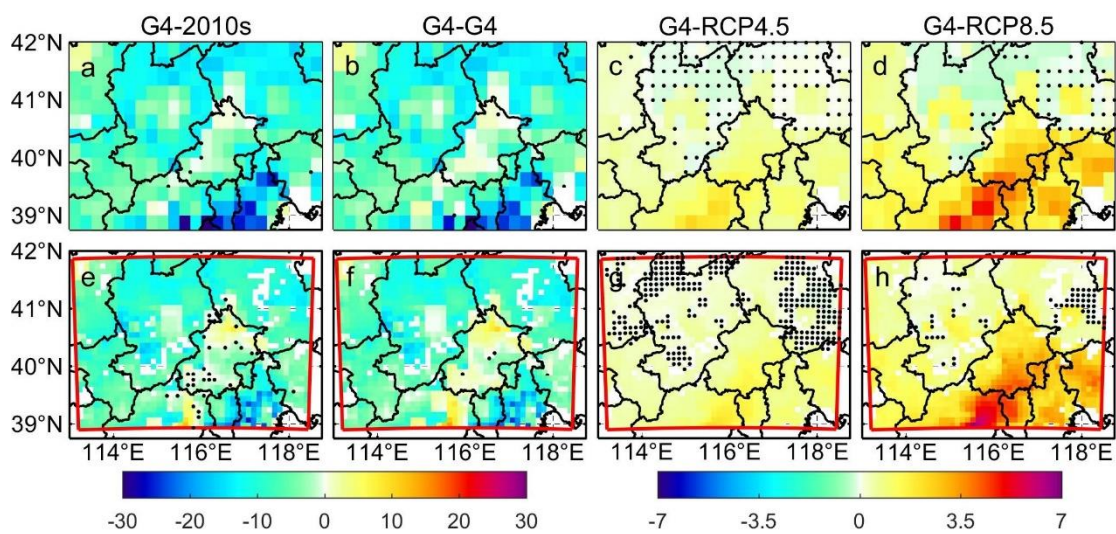
633

Beijing-Tianjin province	G4-2010s		G4-RCP4.5		G4-RCP8.5	
	ISIMIP	WRF	ISIMIP	WRF	ISIMIP	WRF
MIROC-ESM	<b>18.6</b>	-8.1	-17.0	0.8	<b>-35.4</b>	<b>-13.1</b>
MIROC-ESM-CHEM	<b>28.7</b>	<b>-10.2</b>	3.9	-2.2	<b>-33.7</b>	<b>-15.5</b>
HadGEM2-ES	<b>25.7</b>	<b>9.4</b>	<b>-12.5</b>	<b>-13.5</b>	<b>-24.3</b>	<b>-25.3</b>
BNU-ESM	<b>16.4</b>	<b>13.6</b>	-8.6	<b>-10.4</b>	<b>-40.5</b>	<b>-24.4</b>
Ensemble	<b>22.4±2.9</b>	1.2±6.0	<b>-8.6±4.5</b>	<b>-6.3±3.4</b>	<b>-33.5±3.4</b>	<b>-19.6±3.1</b>

634

### 635 3.3 $PM_{2.5}$ in the 2060s

#### 636 3.3.1 $PM_{2.5}$ scenarios in the 2060s



637

638 **Figure 11.** Spatial patterns of ensemble mean  $PM_{2.5}$  concentration difference ( $\mu\text{g}/\text{m}^3$ ) between  
 639 “mitigation” under G4 in the 2060s and reference (a, e), between “mitigation” and “baseline” under  
 640 G4 in the 2060s (b, f), between G4 and RCP4.5 under “mitigation” scenario in the 2060s (c, g), and

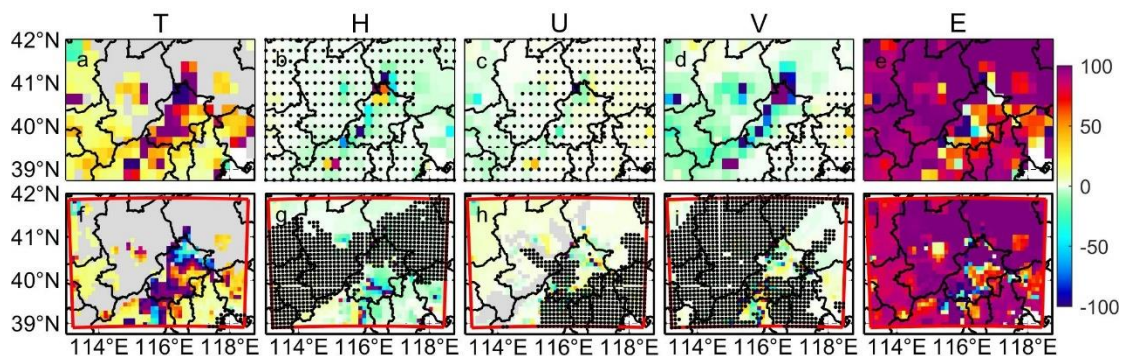
641 between G4 and RCP8.5 under “mitigation” scenario in the 2060s (**d, h**) based on ISIMIP (**a-d**) and  
 642 WRF (**e-h**) results. Excessive collinearity variables have been removed (Fig. S18 shows the results  
 643 without this procedure). Stippling indicates grid points where differences or changes are not  
 644 significant at the 5% significant level according to the Wilcoxon signed rank test.

645

646 We firstly project the change of  $PM_{2.5}$  under G4 and the aerosol mitigation scenario in  
 647 2060s relative to 2010s (Fig. 11a, e). Both ISIMIP and WRF project  $PM_{2.5}$  decreases in  
 648 most areas, especially in Tianjin and Langfang, but  $PM_{2.5}$  decreases more under ISIMIP  
 649 than WRF.  $PM_{2.5}$  concentration decreases by  $7.6 \mu\text{g}/\text{m}^3$  over Beijing-Tianjin province  
 650 in ISIMIP, and decrease by  $5.4 \mu\text{g}/\text{m}^3$  in WRF (Table S3).  $PM_{2.5}$  concentration is  $0.5\text{-}8$   
 651  $\mu\text{g}/\text{m}^3$  higher in northern Beijing under G4 (“mitigation”) than that during the 2010s in  
 652 WRF. To show the impact of emission reductions, we compare the  $PM_{2.5}$  concentration  
 653 between aerosol “baseline” and “mitigation” scenarios under G4 in the 2060s (Fig. 11b,  
 654 11f), and compare the “mitigation”  $PM_{2.5}$  concentration under G4 and the RCP  
 655 scenarios in the 2060s to clarify the effect of geoengineering compared with climate  
 656 warming. Compared with “baseline” scenario,  $PM_{2.5}$  concentration is less under  
 657 “mitigation” scenario as expected in both ISIMIP and WRF under G4 (Fig. 11b, 11f),  
 658 and has a similar spatial pattern with that in Fig. 11a and 11e. Compared with RCP4.5  
 659 and RCP8.5,  $PM_{2.5}$  concentration under G4 are higher over the Beijing-Tianjin province  
 660 in ISIMIP results (Fig. 11c-11d), but with large differences between the 4 ESMs. G4  
 661  $PM_{2.5}$  is simulated greater than in RCP scenarios under HadGEM2-ES and BNU-ESM  
 662 (Fig. S19k, l, o, p), but there are insignificant differences in most areas under the two  
 663 MIROC models (Fig. S19c, d, g, h).  $PM_{2.5}$  concentrations are larger between G4 and  
 664 RCP8.5. WRF simulations shows similar changes in  $PM_{2.5}$  between G4 and RCPs as  
 665 ISIMIP over Beijing-Tianjin province (Fig. 11g-h).

666

### 667 3.3.2 $PM_{2.5}$ meteorological and emissions controls in the 2060s



668

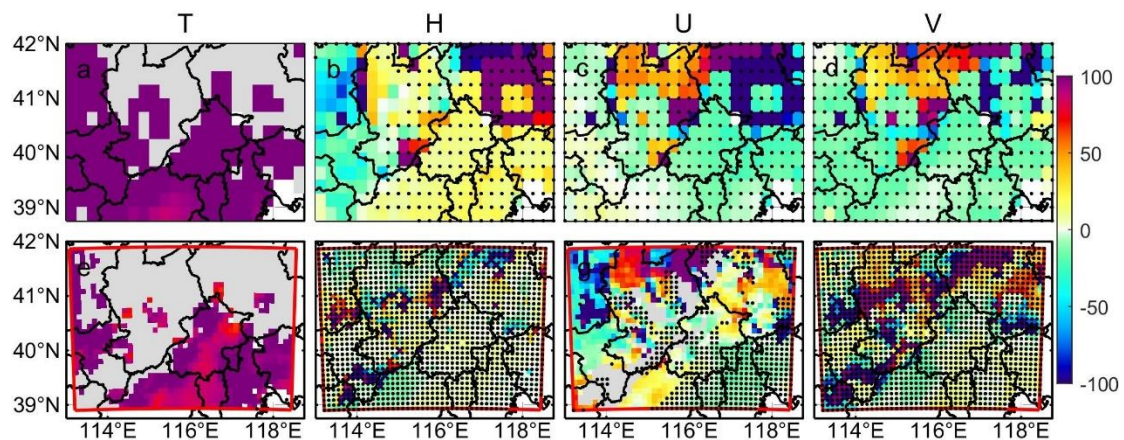
669 **Figure 12.** Contribution of climate factors (temperature/T, humidity/H, zonal wind/U, meridional  
 670 wind/V) and emission (E) to changes in monthly  $PM_{2.5}$  concentration ( $\Delta PM_{2.5}$ ) in 2060s under G4  
 671 (“mitigation”) relative to 2010s. Top figures (**a-e**) are ISIMIP results, and bottom figures (**f-j**) are  
 672 WRF results. Stippling indicates the changes are insignificant at the 5% significant level in the  
 673 Wilcoxon test. The grey areas represent the collinearity in the MLR, and they exist in the panel a, f



674 and h.

675

676 Next, we quantify the contribution of different meteorological factors and  $PM_{2.5}$   
677 emissions to  $\Delta PM_{2.5}$  between G4 (“mitigation”) in the 2060s and the 2010s (Fig. 12).  
678 Both ISIMIP and WRF results show that the increase of temperature and decrease of  
679  $PM_{2.5}$  emission play positive roles in reducing  $PM_{2.5}$  concentration. ISIMIP results (Fig.  
680 12a-e), suggest that the projected increase of temperature could explain 0-20% of the  
681 decrease of  $PM_{2.5}$  concentration, and decrease of  $PM_{2.5}$  emission could explain more  
682 than 90% of changes in  $PM_{2.5}$  concentration differences in most of areas. Changes in  
683 humidity and westerly winds (positive U-wind) do not cause significant changes in  
684  $\Delta PM_{2.5}$ , but projected increases southerly wind (positive V-wind) is detrimental to the  
685 decrease in  $PM_{2.5}$  concentration, and has a 0-10% negative effect on  $\Delta PM_{2.5}$  in  
686 Zhangjiakou. WRF results show similar spatial pattern in effect of temperature and  
687 emission on  $\Delta PM_{2.5}$  with ISIMIP results. Although temperature is projected to increase  
688 over the whole domain (Fig. S22), there are negative contributions on  $\Delta PM_{2.5}$  to the  
689 north of Beijing due to increase of  $PM_{2.5}$  caused by the negative correlation between  
690  $PM_{2.5}$  and its emissions (Fig. S26). The  $\sim 1\text{-}2\%$  increase of humidity leads to  $\sim 10\%$   
691 increase of  $PM_{2.5}$  concentration in the south of Beijing (Fig. 12g), and 0.2-0.3 m/s  
692 decreases of U-wind leads to 0-10% increase of  $PM_{2.5}$  concentration in Zhangjiakou (Fig.  
693 12h). The changes in each factor in ISIMIP and WRF results are shown in Fig. S21 and  
694 Fig. S22, respectively.



695

696 **Figure 13.** Contribution of climate factors (as in Fig. 12) to changes in monthly  $PM_{2.5}$  concentration  
697 in 2060s under G4 with aerosol “mitigation” relative to 2060s under RCP4.5 with aerosol  
698 “mitigation”. Top figures (a-e) are ISIMIP results, and bottom figures (f-j) are WRF results.  
699 Stippling indicates the changes are insignificant at the 5% significant level in the Wilcoxon test. The  
700 grey areas represent the collinearity in the MLR, and they exist in the panel a, f and h.

701

702 Now we explore the contribution of each meteorological factor to  $\Delta PM_{2.5}$  between G4  
703 (“mitigation”) and RCP4.5 (“mitigation”) in the 2060s (Fig. 13). The higher  $PM_{2.5}$   
704 under G4 is mainly caused by the lower temperature. In ISIMIP, lower temperature  
705 explains more than 90% (100% in some places) of the raised  $PM_{2.5}$  relative to RCP4.5,

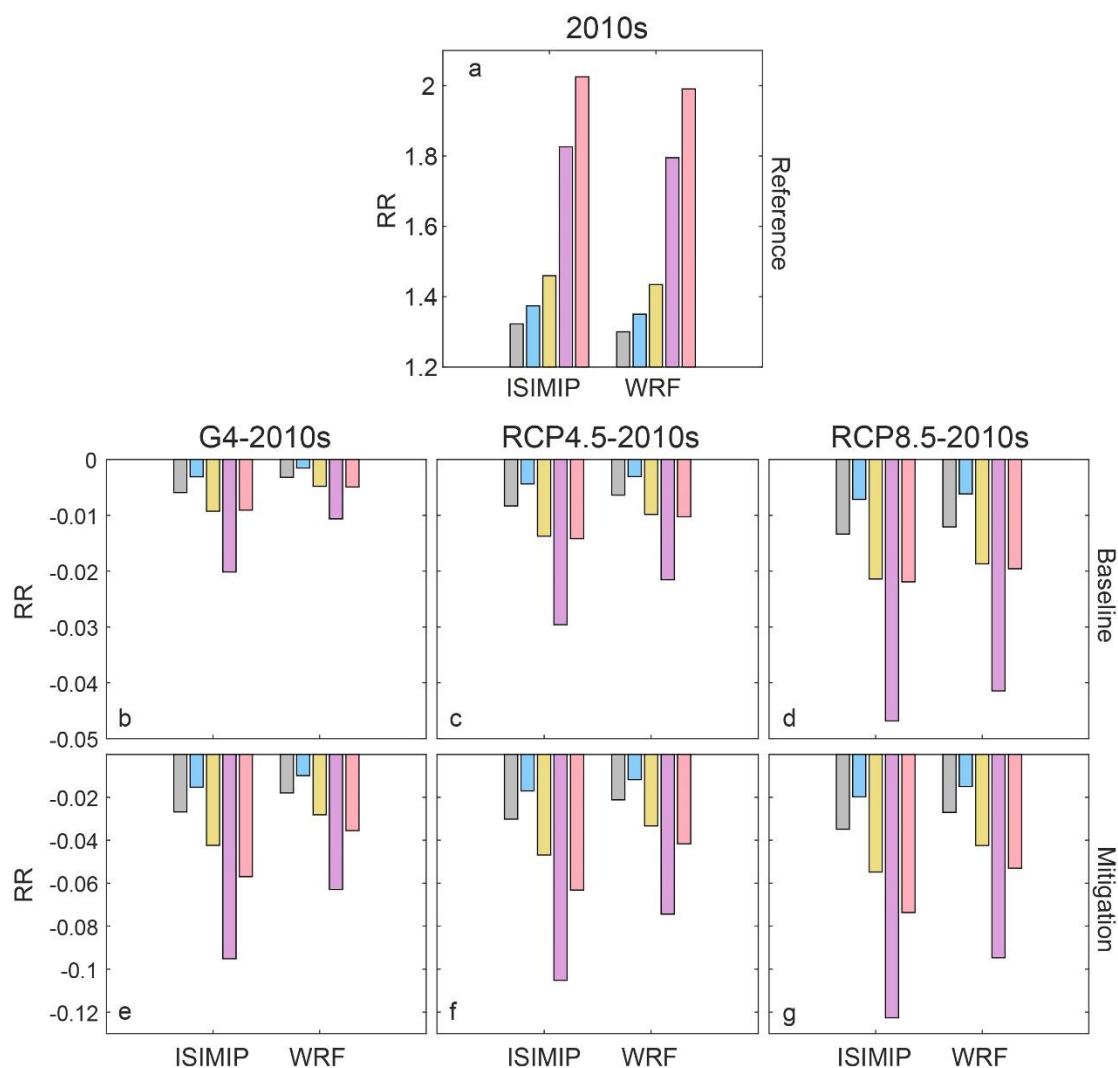
706 although the increase of humidity is also helpful to lower  $PM_{2.5}$  in the western domain  
707 (Fig. 13a-b). Humidity can increase suspended particle mass and coagulation,  
708 promoting deposition (Li et al., 2015). The contribution of differences in U-wind and  
709 V-wind on  $\Delta PM_{2.5}$  is insignificant (Fig. 13c-d). In WRF, the projected lower  
710 temperatures explain more than 70% of the higher  $PM_{2.5}$  under G4 relative to RCP4.5  
711 (Fig. 13e). Although the increase of southerly (V) wind contributes 10-20% to the  
712 higher  $PM_{2.5}$  in the northern domain under HadGEM2-ES and BNU-ESM (Fig. S24),  
713 it is insignificant in the ensemble (Fig. 13h). Decreased westerlies (U wind) explains  
714 about between +100% and -100% of  $PM_{2.5}$  differences (Fig. 13g), since U-wind impacts  
715 vary spatially (Fig. S26).

716

### 717 **3.3.3 $PM_{2.5}$ impact on health risks now and in the 2060s**

718 Changes in RR of  $PM_{2.5}$  for the 5 diseases under the geoengineering and global  
719 warming climate scenarios and different emission scenarios during 2060s relative to  
720 2010s for the Beijing-Tianjin province are shown in Fig. 14. Present-day  $PM_{2.5}$  related  
721 RRs are 1.32 (1.30), 1.37 (1.35), 1.46 (1.43), 1.83 (1.80) and 2.03 (1.99) for chronic  
722 obstructive pulmonary disease (COPD), ischemic heart disease (IHD), lung cancer (LC),  
723 lung respiratory infection (LRI) and stroke according to the ISIMIP (WRF) simulations  
724 (Fig. 14a). RR of LRI is the highest and COPD is the lowest in the five diseases, and  
725 WRF estimates of RR are 0.02-0.03 lower than those of ISIMIP. In both the “baseline”  
726 and “mitigation” emission scenarios, RRs will be lower under G4, RCP4.5 and RCP8.5  
727 compared with the 2010s. Smaller RR reductions occur under G4 than under RCP4.5  
728 and RCP8.5, and ISIMIP simulates larger reductions than WRF. This is because the  
729  $PM_{2.5}$  concentrations from ISIMIP are reduced more than with WRF (Table S3). Under  
730 the “baseline” emission scenario (Fig. 14b-d), the biggest reduction of RR for LRI is  
731 0.047 under RCP8.5 in ISIMIP, and RRs for other diseases are projected to reduce by  
732 no more than 0.02. Under the “mitigation” emission scenario (Fig. 14e-g), reductions  
733 in RRs are 3-6 times greater.





734

735 **Figure 14.** Average population-weighted relative risks of PM<sub>2.5</sub> related 5 diseases in 2010s (a) and  
 736 its changes between G4 and 2010s (b, e), between RCP4.5 and 2010s (c, f) and between RCP8.5  
 737 and 2010s (d, g) in Beijing-Tianjin province based on the ISIMIP and WRF results, respectively.  
 738 PM<sub>2.5</sub> concentration is based on the “baseline” emissions under G4, RCP4,5 and RCP8.5 in the  
 739 middle 3 figures (b-d), and it is based on the “mitigation” emissions under G4, RCP4,5 and RCP8.5  
 740 in the bottom 3 figures (e-g).

741

## 742 4. Discussion

### 743 4.1 Apparent temperature

744

745 Both ISIMIP and WRF can reproduce the observed (CN05.1) spatial patterns and  
 746 seasonal variabilities of apparent temperature in the region around Beijing. WRF shows  
 747 warm biases in AP during all months relative to CN05.1 due to warmer temperatures in  
 748 urban areas, with the exception of BNU-ESM and HadGEM2-ES driven summers (Fig.  
 749 S13). Both ISIMIP and WRF tend to overestimate population weighted NdAP<sub>32</sub> by

750 370% and 590%, respectively. These large discrepancies are due to relatively small  
751 overestimates of the likelihood of the tails of the probability distributions which leads  
752 to a dramatic increase in the frequency of extreme climate events (Dimri et al., 2018;  
753 Huang et al., 2021). AP is about 1.5°C warmer than 2 m temperature over the Beijing  
754 and Tianjin urban areas in summer due to higher vapor pressures amplifying warmer  
755 urban temperatures, and this is despite humidity being lower over the cities. Under high  
756 humidity conditions, a slight increase in temperature will cause a large increase in heat  
757 stress (Li et al., 2018; Luo and Lau, 2019). AP is nearly 4°C colder than 2 m temperature  
758 in winter due to wind speed (Fig. 2d). Differences between AP and 2 m temperature  
759 (AP-T) during summer are greater in urban areas than neighboring rural areas.

760

761 The apparent temperatures in Beijing Tianjin urban areas under G4 in the 2060s are  
762 simulated to be 1°C and 2.5°C lower than RCP4.5 and RCP8.5, although AP would be  
763 higher than in the recent past. The cooling effect of G4 relative to RCP4.5 and RCP8.5  
764 is greatest under HadGEM2-ES (Fig. S14, S15), due to the ESM having largest  
765 temperature differences between scenarios (Wang et al., 2022). WRF downscaling  
766 produces reduced seasonality in AP compared with ISIMIP, and WRF produces  
767 relatively cooler summers and warmer winters than ISIMIP, and so much less  
768 differences in apparent temperature ranges (Fig. 15). Differences in AP between G4 and  
769 the RCP scenarios are mainly driven by temperature. In all scenarios and downscalings  
770 AP rises faster than the temperature due to decreased wind speeds in the future (Li et  
771 al., 2018; Zhu et al., 2021) but mainly because of rises in vapor pressure driven by  
772 rising temperatures. This effect occurs despite the general drying expected under solar  
773 geoengineering (Bala et al., 2008; Yu et al., 2015).

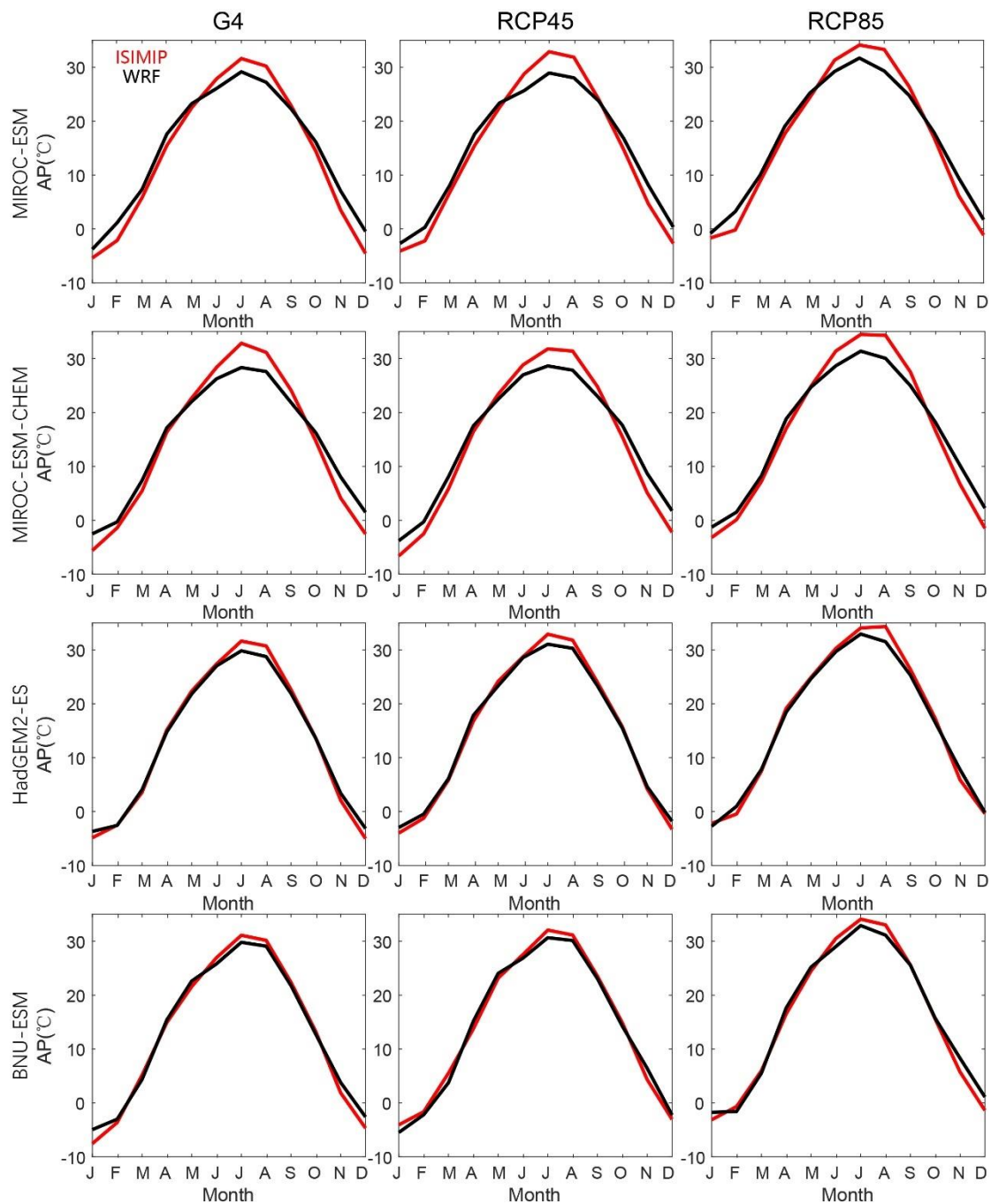
774

775 The NdAP\_32 under G4 is projected to decrease by 8.6 days per year by ISIMIP and  
776 6.3 days per year by WRF relative to RCP4.5 for Beijing-Tianjin Province. Much larger  
777 reductions in NdAP\_32 of 33.5 days per year (ISIMIP) and 19.6 days per year (WRF)  
778 are projected relative to RCP8.5. Differences between scenarios in frequency of  
779 dangerously hot days are far larger using ISIMIP statistical downscaling than using  
780 WRF. This is another impact of the reduced seasonality of WRF compared with ISIMIP  
781 (Fig. 15).

782

783 The higher resolution WRF simulation produces a much larger range of apparent  
784 temperatures across the domain than CN05.1 and ISIMIP downscaling. This increased  
785 variability makes reaching a statistical significance threshold more challenging for  
786 WRF than ISIMIP results. Despite this, the ESM-driven differences in WRF output are  
787 less than from ISIMIP, reflecting the physically based processes in the dynamic WRF  
788 simulation. This reduces the impact of differences in ESM forcing at the domain  
789 boundaries with WRF compared with the statistical bias correction and downscaling  
790 methods. Although there are some uncertainties between models and downscaling  
791 methods, G4 SAI can not only reduce the mean apparent temperature but also decrease  
792 the probability of PDF tails (extreme events) in summer.

793



794

795 **Figure 15.** Seasonal cycles of apparent temperature from MIROC-ESM, MIROC-ESM-CHEM,  
 796 HadGEM2-ES and BNU-ESM under G4, RCP4.5 and RCP8.5 in Beijing-Tianjin urban areas during  
 797 2060s based on ISIMIP (red) and WRF (black) methods.

798

## 799 **4.2 PM<sub>2.5</sub>**

800 We established a set spatially gridded MLR models based on the 4 ESMs downscaled  
 801 variables under ISIMIP and WRF. The meteorological factors impact PM<sub>2.5</sub> in complex  
 802 ways, but the simple spatially gridded MLR models display enough skill to make some  
 803 illustrative projections of future PM<sub>2.5</sub> explaining about 70% of the variance during the  
 804 historical period. PM<sub>2.5</sub> concentration is correlated with emissions and anti-correlated

805 with temperature in most parts of the domain (Fig. S25-S26). Increased turbulence  
806 increases diffusion of PM<sub>2.5</sub> (Yang et al., 2016), and higher temperatures increase  
807 evaporation losses (Liu et al., 2015) of ammonium nitrate (Chuang et al., 2017), and  
808 other components (Wang et al., 2006). Humidity may have both positive and negative  
809 effects on PM<sub>2.5</sub> (Chen et al., 2020). It causes more water vapor to adhere to the surface  
810 of PM<sub>2.5</sub>, thereby increasing its mass concentration and facilitating aerosol growth  
811 (Cheng et al., 2017; Liao et al., 2017). However, when the humidity exceeds a certain  
812 threshold, coagulation and particle mass increases rapidly, promoting deposition (Li et  
813 al., 2015). So, the slope coefficients between PM<sub>2.5</sub> and humidity are positive in low  
814 humidity areas, including southern plain and the Beijing-Tianjin province, but negative  
815 in some northern mountain areas (Fig. S25, S26).

816

817 There are large spatial differences in wind speed and direction impacts on PM<sub>2.5</sub>. Yang  
818 et al. (2016) found that weaker northerly and westerly winds tend to increase the PM<sub>2.5</sub>  
819 concentration in northern and eastern China, respectively. The effects of wind direction  
820 depend on the distribution of emitted PM<sub>2.5</sub> and the condition of the underlying surface  
821 (Chen et al., 2020). Most sources of PM<sub>2.5</sub> lie to the south of our domain, relatively  
822 clean conditions prevail to the north, so northerly winds tend to advect clean air, while  
823 southerlies bring high concentrations of aerosols. Weak winds tend to increase PM<sub>2.5</sub>  
824 and smog formation due to sinking air and weak diffusion (Su et al., 2017; Yang et al.,  
825 2017).

826

827 Xu et al. (2021) projected 2030 PM<sub>2.5</sub> concentrations will decrease by 8.8% and 5.5%  
828 under RCP4.5 and RCP8.5 respectively relative to 2015. Wang et al. (2021) also  
829 projected decreasing trends in China under RCP4.5 and RCP8.5 during 2030-2050.  
830 There were seasonal changes in PM<sub>2.5</sub> concentration differences between RCP4.5/8.5  
831 scenarios and the historical scenario near the Bohai Sea (Dou et al., 2021). However,  
832 there are also some simulations where PM<sub>2.5</sub> concentrations increase in warmer climates.  
833 Hong et al. (2019) suggest that annual mean PM<sub>2.5</sub> concentrations will increase 1-8  
834  $\mu\text{g}/\text{m}^3$  in an area including Beijing and Tianjin under RCP4.5 during 2046-2050,  
835 compared with 2006-2010. These inconsistent responses are mainly caused by the  
836 differences in the selection of ESMs, chemical transport models and climate/emission  
837 scenarios. Different RCP scenarios not only correspond to different future climate states,  
838 but also have different anthropogenic emissions of air pollutants. In our study, we do  
839 not consider the PM<sub>2.5</sub> emission differences between RCP4.5 and RCP8.5, and instead  
840 applied the ECLIPSE PM<sub>2.5</sub> emission scenarios in our MLR projection.

841

842 Emissions reductions are expected to play the dominant role in the decrease of PM<sub>2.5</sub>  
843 concentrations under G4 aerosol “mitigation” in 2060s (Fig. 12). Meteorological  
844 changes under the different future scenarios make much smaller changes as evidenced  
845 by the scenarios using “baseline” – that is present day PM<sub>2.5</sub> emissions, with decreases  
846 in mean annual concentration of 1.0 (1.3), 1.8 (2.0), 3.3 (3.2)  $\mu\text{g}/\text{m}^3$  over Beijing-

847 Tianjin province under G4, RCP4.5 and RCP8.5 with WRF (ISIMIP), (Table S3), which  
848 are mainly caused by the temperature increases (Fig. 13). The negative relationships  
849 between emission and PM<sub>2.5</sub> concentration result in the increase of PM<sub>2.5</sub> under G4  
850 (“mitigation”) relative to 2010s in the north of Beijing with WRF. This may be due to  
851 changes in PM<sub>2.5</sub> out of the domain being opposite to those in domain during the MLR  
852 fitting period, since relocation of polluting sources from the urban areas mainly to the  
853 west, was occurring over the calibration period. The accuracy of PM<sub>2.5</sub> emission data is  
854 also crucial for training MLR models, and PM<sub>2.5</sub> data was sparse before 2013, relying  
855 on reconstructions based on satellite optical depth estimates. Although both increase of  
856 temperature and decrease of emission explain more than 90% of the decrease in PM<sub>2.5</sub>  
857 in most areas, there are large spatial differences due to wind and humidity. On the one  
858 hand, there is uncertainty in the differences in changes of wind speed and humidity  
859 between different ESMs and downscaling methods; on the other hand, the complex  
860 physical relationship between them and PM<sub>2.5</sub> also increases uncertainties. Reductions  
861 in PM<sub>2.5</sub> in the future are projected to decrease PM<sub>2.5</sub> related health issues, although its  
862 effect on different diseases are different. Changes in PM<sub>2.5</sub> related risk between G4 and  
863 RCPs are from 1-3%, with PM<sub>2.5</sub> emissions policy dominating differences over climate  
864 scenario.

865

866 There are some differences in projecting PM<sub>2.5</sub> concentration between WRF and ISIMIP  
867 methods. Compared to the 2010s reference, PM<sub>2.5</sub> concentration in ISIMIP are  
868 projected to decrease more than using WRF in G4 under the “mitigation” scenario  
869 during the 2060s over the Tianjin province (Fig. 11a, e). However, the spatial patterns  
870 of changes in PM<sub>2.5</sub> concentration between G4 and RCP4.5/8.5 under the “mitigation”  
871 scenario during 2060s are similar (Fig. 11c-d, g-h). This means that the effects of  
872 different downscaled methods on projecting PM<sub>2.5</sub> are small if we only consider the  
873 climate change alone without considering emissions changes. Due to the larger  
874 regression coefficient of emissions in the MLR under the ISIMIP method (Fig. S25,  
875 S26), the negative changes in PM<sub>2.5</sub> concentration are larger between “mitigation” and  
876 baseline under G4 during 2060s than that under the WRF method. Correspondingly, the  
877 ISIMIP method has a greater reduction in PM<sub>2.5</sub> related RR than WRF under three future  
878 climate scenarios during the 2060s.

879

880 Eastham et al. (2018) deduced from experiments using 1 Tg/yr SAI in a coupled  
881 chemistry-transport model directly simulating atmospheric chemistry, transport,  
882 radiative transfer of UV, emissions, and loss processes, that per unit mass emitted,  
883 surface-level emissions of sulfate result in 25 times greater population exposure to  
884 PM<sub>2.5</sub> than emitting the same aerosol into the stratosphere. The G4 experiment specifies  
885 5 Tg/yr injection rate, which over our domain would equate to 1450 t/yr if it was  
886 deposited uniformly globally (which it certainly would not be). Reducing this by the  
887 1/25 factor amounts to 58 t/yr which can be compared with present PM<sub>2.5</sub> emissions of  
888 around  $3.3 \times 10^5$  t/year in our domain. If we consider the aerosol deposition under G4  
889 scenarios, PM<sub>2.5</sub> concentration will be 0-1  $\mu\text{g}/\text{m}^3$  higher than that without due to

890 deposition of the SAI aerosols (Fig. S27), and RR is projected to increase by 0.01% for  
891 Beijing-Tianjin province (Table S4). This comparison suggests that tropospheric  
892 emissions will be much more important for human health in our domain than from the  
893 SAI specified by G4.

894

895 The most important change in  $PM_{2.5}$  will come from emissions reductions, with the  
896 different weather conditions under both G4 and RCP scenarios making relatively little  
897 practical differences in concentrations.  $PM_{2.5}$  concentration is expected to decrease  
898 significantly (ISIMIP:  $-7.6\mu g/m^3$ , WRF:  $-5.4\mu g/m^3$ ) in the Beijing-Tianjin province,  
899 but they will still not meet either Chinese or international standards. The temperature  
900 under G4 is lower than that under RCP4.5 and RCP8.5 scenarios, which makes the  
901  $PM_{2.5}$  concentration under G4 higher. But the difference in  $PM_{2.5}$  between the two is  
902 small and even within uncertainty due to projected differences in humidity and wind.  
903 Potentially improved estimates from more complex models such as WRF-Chem,  
904 CMAQ and GEOS-Chem over the simple MLR methods used here will be of limited  
905 value unless the differences between the ESM driving these models is reduced. It can  
906 be confirmed that emission policies based on the 13<sup>th</sup> Five Year Plan are not enough,  
907 and higher emission standards need to be developed for a healthy living environment.

908

909 Our study did not consider the impacts of socio-economic pathways on  $PM_{2.5}$  future  
910 emissions, instead we explore the meteorological differences between the SAI G4  
911 scenario and the greenhouse gas RCP4.5/RCP8.5 on  $PM_{2.5}$  concentrations.  $PM_{2.5}$   
912 emissions were defined by the uncontrolled (“baseline”) and a scenario where  
913 technological intervention (“mitigation”) reduces emissions. There are some limitations  
914 in our study. Firstly, the HTAP\_V3 dataset only includes anthropogenic  $PM_{2.5}$  emission,  
915 not natural  $PM_{2.5}$  emission. Natural  $PM_{2.5}$  will also change in the future under changing  
916 climate. The sources of natural  $PM_{2.5}$  include the sandstorms that sometimes occur in  
917 spring as extreme winds mobilize dry unvegetated soils. These relatively extreme  
918 conditions are difficult to simulate in ESM and subject to land use policy e.g., the  
919 numerous ecosystem service measures undertaken by China over the last five decades  
920 (Miao et al.,2015). Secondly, although  $PM_{2.5}$  concentration includes both primary and  
921 secondary  $PM_{2.5}$  during model training, we do not consider the precursor gases for  
922 secondary  $PM_{2.5}$  directly. The sensitivity of MLR may diminish at the high  $PM_{2.5}$  values  
923 when secondary  $PM_{2.5}$  dominates the variability of total  $PM_{2.5}$  (Upadhyay et al., 2018).  
924 Thirdly, we only consider the effect of dominant near-surface meteorological variables  
925 on the  $PM_{2.5}$ . However, the vertical transport of pollutants related to vertical  
926 atmospheric stability should not be ignored (Lo et al., 2006; Wu et al., 2005), and this  
927 may contribute to the differences in RCP4.5 scenario from our MLR model and more  
928 sophisticated simulations (Fig. S7). Finally, although it is insignificant for the Beijing  
929 and Tianjin provinces, the MLR model suffers collinearity problems in some areas.  
930 These factors play smaller roles as we are mainly considering changes in  $PM_{2.5}$   
931 concentration between different climate scenarios. Nevertheless, projection for changes

932 in PM<sub>2.5</sub> between SAI scenarios and per greenhouse gas scenarios would be valuable  
933 for global air quality impacts from geoengineering.

934

## 935 **5. Conclusion**

936 Our study on thermal comfort and aerosol pollution under geoengineering scenarios for  
937 the Beijing megalopolis may be useful across the developing world, which is expected  
938 to suffer disproportionate climate impact damages relative the global mean, while also  
939 undergoing rapid urbanization. Assessing health impacts and mortality due to heat  
940 stress and PM<sub>2.5</sub> under greenhouse gas scenarios should consider urbanization and the  
941 change to concrete surfaces from vegetation that leads to differences in heat capacities,  
942 rates of evapotranspiration, and hence humidity and apparent temperature. These  
943 require downscaled analyses, accurate meteorological and high-resolution land surface  
944 datasets, and industrial development scenarios.

945

946 In our analysis we assumed the urban area did not change over time, and also that  
947 population remains distributed as in the recent past. This may be reasonable in the  
948 highly developed and relatively mature greater Beijing-Tianjin region but should be  
949 considered in rapidly urbanizing regions elsewhere. There certainly will be changes  
950 over time in the radiative cooling from surface pollution sources. PM<sub>2.5</sub> is a health issue  
951 in many developing regions (Ran et al., 2023), but as wealth increases efforts to curb  
952 air pollution generally clean the air. This has clear health benefits, but also removes  
953 aerosols from the troposphere that cool the surface. The urban areas that have higher  
954 apparent temperatures at present are also the areas with greatest aerosol load and hence  
955 greatest cooling. Once that is removed direct radiation, air temperatures and apparent  
956 temperatures will all rise – by several degrees (Wang et al., 2016). So, a future more  
957 comprehensive health impact study would include both the negative health impacts of  
958 aerosol pollution and the potential cooling effects those aerosols produce. Additionally,  
959 the formulation of apparent temperature used does not consider the effect of radiation  
960 on human comfort (Kong and Huber, 2022). When PM<sub>2.5</sub> levels are high there is no  
961 shade because the sky is milky-white, similarly SAI will brighten the sky (Kravitz et  
962 al., 2012). Comfort is increased in clear sky conditions when shade is readily found.

963

964 The changes simulated to relative risk from increased PM<sub>2.5</sub> under the G4 SAI scenario  
965 are about 1-3% worse than under RCP4.5, mainly because of lower temperatures under  
966 G4. The difference this would make to the overall health burden under SAI depends on  
967 the range of other impacts that include changes in apparent temperature we discuss. G4  
968 reduces the number of days with AP>32 (when extreme caution is advised) by 6-8 per  
969 year relative to RCP4.5 and by 20-34 relative to RCP8.5. But G4 itself will still increase  
970 these extreme caution days by 1-20 relative to conditions in the 2010s. Lowering PM<sub>2.5</sub>  
971 emissions will increase ground temperatures and the associated risk of dangerous  
972 apparent temperatures will also increase rapidly as the distribution of temperatures is  
973 shifted making presently rare hot events into much more frequent heat waves.

974 **Code and data availability**

975 All ESM data used in this work are available from the Earth System Grid Federation  
976 (WCRP, 2021; <https://esgf-node.llnl.gov/projects/cmip6>, last access: 14 July 2021).  
977 The WRF and ISIMIP bias-corrected and downscaled results are available for the  
978 authors on request. WRF and ISIMIP codes are freely available at the references cited  
979 in the methods sections.

980 **Supplement link**

981 The link to the supplement will be included by Copernicus.

982 **Author contribution**

983 JCM and LZ designed the experiments, JW performed the simulations. All the authors  
984 wrote the manuscript.

985 **Competing interests**

986 The authors declare that they have no conflict of interest.

987 **Disclaimer**

988 Publisher's note: Copernicus Publications remains neutral with regard to jurisdictional  
989 claims in published maps and institutional affiliations.

990 **Special issue statement:**

991 This article is part of the special issue "Resolving uncertainties in solar geoengineering  
992 through multi-model and large-ensemble simulations (ACP/ESD inter-journal SI)". It  
993 is not associated with a conference.

994 **Acknowledgements**

995 We thank the editor and two constrictive referees for improving the manuscript. This  
996 work relies on the climate modeling groups participating in the Geoengineering Model  
997 Intercomparison Project and their model development teams; the CLIVAR/WCRP  
998 Working Group on Coupled Modeling for endorsing the GeoMIP; and the scientists  
999 managing the earth system grid data nodes who have assisted with making GeoMIP  
1000 output available. This research was funded by the National Key Science Program for  
1001 Global Change Research (2015CB953602).

1002



## 1003 **References**

- 1004 Burnett, R., Pope III, C., Ezzati, M., Olives, C., Lim, S., Mehta, S., Shin, H., Singh, G.,  
1005 Hubbell, B., Brauer, M., Anderson, A., Smith, K., Balmes, J., Bruce, N., Kan, H.,  
1006 Laden, F., Prüss-Ustün, A., Turner, M., Gapstur, S., Diver, W., and Cohen, A.: An  
1007 Integrated Risk Function for Estimating the Global Burden of Disease Attributable  
1008 to Ambient Fine Particulate Matter Exposure, *Environ., Health Perspect.*, 122, 397-  
1009 403, <https://doi.org/10.1289/ehp.1307049>, 2014.
- 1010 Bala, G., Duffy, P. B., Taylor, K. E.: Impact of geoengineering schemes on the global  
1011 hydrological cycle, *Proc. Natl. Acad. Sci. USA*, 105 (22), 7664-7669,  
1012 <https://doi.org/10.1073/pnas.0711648105>, 2008.
- 1013 Chen, Z., Cai, J., Gao, B., Xu, B., Dai, S., He, B., Xie, X.: Detecting the causality  
1014 influence of individual meteorological factors on local PM<sub>2.5</sub> concentrations in the  
1015 Jing-Jin-Ji region, *Sci. Rep.*, 7, 40735, <https://doi.org/10.1038/srep40735>, 2017.
- 1016 Chen, Z., Chen, D., Kwan, M.-P., Chen, B., Gao, B., Zhuang, Y., Li, R., and Xu, B.: The  
1017 control of anthropogenic emissions contributed to 80 % of the decrease in  
1018 PM<sub>2.5</sub> concentrations in Beijing from 2013 to 2017, *Atmos. Chem. Phys.*, 19, 13519–  
1019 13533, <https://doi.org/10.5194/acp-19-13519-2019>, 2019.
- 1020 Chen, Z., Chen, D., Zhao, C., Kwan, M., Cai, J., Zhuang, Y., Zhao, B., Wang, X., Chen,  
1021 B., Yang, J., Li, R., He, B., Gao, B., Wang, K., and Xu, B.: Influence of  
1022 meteorological conditions on PM<sub>2.5</sub> concentrations across China: A review of  
1023 methodology and mechanism, *Environ. Int.*, 139, 105558,  
1024 <https://doi.org/10.1016/j.envint.2020.105558>, 2020.
- 1025 Chen, Z., Xie, X., Cai, J., Chen, D., Gao, B., He, B., Cheng, N., and Xu, B.:  
1026 Understanding meteorological influences on PM<sub>2.5</sub> concentrations across China: a  
1027 temporal and spatial perspective, *Atmos. Chem. Phys.*, 18, 5343–5358,  
1028 <https://doi.org/10.5194/acp-18-5343-2018>, 2018.
- 1029 Cheng, L., Meng, F., Chen, L., Jiang, T., and Su, L.: Effects on the haze pollution from  
1030 autumn crop residue burning over the Jing-Jin-Ji Region, *China Environ. Sci.*, 37,  
1031 2801–2812, 2017.
- 1032 Chi, X., Li, R., Cubasch, U., Cao, W.: The thermal comfort and its changes in the 31  
1033 provincial capital cities of mainland China in the past 30 years, *Theor. Appl.*  
1034 *Climatol.*, 132(1-2), 599–619, 2018.
- 1035 Chuang, M., Chou, C., Lin, N., Takami, A., Hsiao, T., Lin, T., Fu, J., Pani, S., Lu, Y., and  
1036 Yang, T.: A simulation study on PM<sub>2.5</sub> sources and meteorological characteristics at  
1037 the northern tip of Taiwan in the early stage of the Asian haze period, *Aerosol Air*  
1038 *Qual. Res.*, 17, 3166-3178, <https://doi.org/10.4209/aaqr.2017.05.0185>, 2017.
- 1039 Collins, W. J., Bellouin, N., Doutriaux-Boucher, M., Gedney, N., Halloran, P., Hinton,  
1040 T., Hughes, J., Jones, C. D., Joshi, M., Liddicoat, S., Martin, G., O'Connor, F., Rae,  
1041 J., Senior, C., Sitch, S., Totterdell, I., Wiltshire, A., Woodward, S.: Development  
1042 and evaluation of an Earth-System model – HadGEM2, *Geosci. Model Dev.*, 4,  
1043 1051–1075, <https://doi.org/10.5194/gmd-4-1051-2011>, 2011.
- 1044 Curry, C. L., Sillmann, J., Bronaugh, D., Alterskjaer, K., Cole, J. N. S., Ji, D., Kravitz,  
1045 B., Kristjánsson, J. E., Moore, J. C., Muri, H., Niemeier, U., Robock, A., Tilmes, S.,

1046 and Yang, S.: A multimodel examination of climate extremes in an idealized  
1047 geoengineering experiment, *J. Geophys. Res.-Atmos.*, 119, 3900–3923,  
1048 <https://doi.org/10.1002/2013JD020648>, 2014.

1049 Dimri, A. P., Kumar, D., Choudhary, A., Maharana, P.: Future changes over the  
1050 Himalayas: Maximum and minimum temperature, *Global and Planetary Change*,  
1051 162, 212–234, <https://doi.org/10.1016/j.gloplacha.2018.01.015>, 2018.

1052 Dou, C., Ji, Z., Xiao, Y., Zhu, X., and Dong, W.: Projections of air pollution in northern  
1053 China in the two RCPs scenarios, *Remote Sens.*, 13, 3064,  
1054 <https://doi.org/10.3390/rs13163064>, 2021.

1055 Eastham, D., Weisenstein, D., Keith, D., and Barrett, A.: Quantifying the impact of  
1056 sulfate geoengineering on mortality from air quality and UV-B exposure, *Atmos.*  
1057 *Environ.*, 187, 424–434. DOI: <http://dx.doi.org/10.1016/j.atmosenv.2018.05.047>,  
1058 2018.

1059 Fan, M., Zhang, Y., Lin, Y., Cao, F., Sun, Y., Qiu, Y., Xing, G., Dao, X., and Fu, P.:  
1060 Specific sources of health risks induced by metallic elements in PM<sub>2.5</sub> during the  
1061 wintertime in Beijing, China, *Atmos. Environ.*, 246, 118112,  
1062 <https://doi.org/10.1016/j.atmosenv.2020.118112>, 2021.

1063 Fischer, E., and Knutti, R.: Robust projections of combined humidity and temperature  
1064 extremes, *Nat. Clim. Change*, 3, 126–130, <https://doi.org/10.1038/nclimate1682>,  
1065 2013.

1066 Foley, K. M., Roselle, S. J., Appel, K. W., Bhave, P. V., Pleim, J. E., Otte, T. L., Mathur,  
1067 R., Sarwar, G., Young, J. O., Gilliam, R. C., Nolte, C. G., Kelly, J. T., Gilliland, A.  
1068 B., and Bash, J. O.: Incremental testing of the Community Multiscale Air Quality  
1069 (CMAQ) modeling system version 4.7, *Geosci. Model Dev.*, 3, 205–226,  
1070 <https://doi.org/10.5194/gmd-3-205-2010>, 2010.

1071 Fu, J., Jiang, D., Huang, Y.: 1 km Grid Population Dataset of China, *Digital Journal of*  
1072 *Global Change Data Repository*, <https://doi.org/10.3974/geodb.2014.01.06.V1>,  
1073 2014.

1074 Garcia, F. C., Bestion, E., Warfield, R., Yvon-Durocher, G.: Changes in temperature alter  
1075 the relationship between biodiversity and ecosystem functioning, *Proc. Natl. Acad.*  
1076 *Sci. U.S.A.*, 115, 10989–10999, <https://doi.org/10.1073/pnas.1805518115>, 2018.

1077 Grinsted, A., Moore, J., and Jevrejeva, S.: Projected Atlantic tropical cyclone threat from  
1078 rising temperatures, *PNAS*, 110, 5369–5373, <https://doi/10.1073/pnas.1209980110>,  
1079 2013.

1080 Grundstein, A. and Dowd, J.: Trends in extreme apparent temperatures over the United  
1081 States, 1949–2010, *J. Appl. Meteorol. Climatol.*, 50(8), 1650–1653,  
1082 <https://doi.org/10.1175/JAMC-D-11-063.1>, 2011.

1083 Guan, W., Zheng, X., Chung, K., and Zhong, N.: Impact of air pollution on the burden  
1084 of chronic respiratory diseases in China: time for urgent action, *Lancet*, 388, 1939–  
1085 1951, [https://doi.org/10.1016/S0140-6736\(16\)31597-5](https://doi.org/10.1016/S0140-6736(16)31597-5), 2016.

1086 Guo, L., Zhang, Y., Lin, H., Zeng, W., Liu, T., Xiao, J., Rutherford, S., You, J., Ma, W.:  
1087 The washout effects of rainfall on atmospheric particulate pollution in two Chinese  
1088 cities, *Environ. Pollut.*, 215, 195–202, <https://doi.org/10.1016/j.envpol.2016.05.003>,  
1089 2016.

1090 Han, J., Wang, J., Zhao, Y., Wang, Q., Zhang, B., Li, H., and Zhai, J.: Spatio-temporal  
1091 variation of potential evapotranspiration and climatic drivers in the Jing-Jin-Ji region,  
1092 North China, *Agric. For. Meteorol.*, 256, 75-83,  
1093 <https://doi.org/10.1016/j.agrformet.2018.03.002>, 2018.

1094 Hempel, S., Frieler, K., Warszawski, L., Schewe, J., and Piontek, F.: A trend-preserving  
1095 bias correction – the ISI-MIP approach, *Earth Syst. Dynam.*, 4, 219–236,  
1096 <https://doi.org/10.5194/esd-4-219-2013>, 2013.

1097 Hersbach, H., Bell, B., Berrisford, P., Biavati, G., Horányi, A., Muñoz Sabater, J.,  
1098 Nicolas, J., Peubey, C., Radu, R., Rozum, I., Schepers, D., Simmons, A., Soci, C.,  
1099 Dee, D., Thépaut, J-N.: ERA5 hourly data on pressure levels from 1979 to present,  
1100 Copernicus Climate Change Service (C3S) Climate Data Store (CDS),  
1101 <https://doi.org/10.24381/cds.bd0915c6>, 2018.

1102 Ho, H. C., Knudby, A., Xu, Y., Hodul, M., Aminipouri, M.: A comparison of urban heat  
1103 islands mapped using skin temperature, air temperature, and apparent temperature  
1104 (Humidex), for the greater Vancouver area, *Science of The Total Environment*, 544,  
1105 929-938, <https://doi.org/10.1016/j.scitotenv.2015.12.021>, 2016.

1106 Hong, C., Zhang, Q., Zhang, Y., Davis, S., Tong, D., Zheng, Y., Liu, Z., Guan, D., He,  
1107 K., and Schellnhuber, H. J.: Impacts of climate change on future air quality and  
1108 human health in China, *PNAS*, 116, 17193-17200,  
1109 <https://doi.org/10.1073/pnas.1812881116>, 2019.

1110 Huang, J., Li, Q., Song, Z.: Historical global land surface air apparent temperature and  
1111 its future changes based on CMIP6 projections, *Science of The Total Environment*,  
1112 816, 151656, <https://doi.org/10.1016/j.scitotenv.2021.151656>, 2021.

1113 IPCC, 2021. Climate change 2021: the physical science basis. In: Masson-Delmotte, V.,  
1114 Zhai, P., Pirani, A., Connors, S.L., Péan, C., Berger, S., Caud, N., Chen, Y., Goldfarb,  
1115 L., Gomis, M.I., Huang, M., Leitzell, K., Lonnoy, E., Matthews, J.B.R., Maycock,  
1116 T.K., Waterfiel, T., Yelekçi, O., Yu, R., B.Z. (Eds.), *Contribution of Working  
1117 Group I to the Sixth Assessment Report of the Intergovernmental Panel on Climate  
1118 Change*. Cambridge University Press In Press.

1119 Jacobs, S. J., Pezza, A. B., Barras, V., Bye, J., Vihma, T.: An analysis of the  
1120 meteorological variables leading to apparent temperature in Australia: present  
1121 climate, trends, and global warming simulations, *Glob. Planet. Chang.*, 107, 145–  
1122 156, 2013.

1123 Janssens-Maenhout, G., Crippa, M., Guizzardi, D., Dentener, F., Muntean, M., Pouliot,  
1124 G., Keating, T., Zhang, Q., Kurokawa, J., Wankmüller, R., Denier van der Gon, H.,  
1125 Kuenen, J. J. P., Klimont, Z., Frost, G., Darras, S., Koffi, B., and Li, M.: HTAP\_v2.2:  
1126 a mosaic of regional and global emission grid maps for 2008 and 2010 to study  
1127 hemispheric transport of air pollution, *Atmos. Chem. Phys.*, 15, 11411-11432,  
1128 <https://doi.org/10.5194/acp-15-11411-2015>, 2015.

1129 Ji, D., Fang, S., Curry, C. L., Kashimura, H., Watanabe, S., Cole, J. N. S., Lenton, A.,  
1130 Muri, H., Kravita, B., Moore, J. C.: Extreme temperature and precipitation response  
1131 to solar dimming and stratospheric aerosol geoengineering, *Atmospheric Chemistry  
1132 and Physics*, 18, 10133-10156, <https://doi.org/10.5194/acp-18-10133-2018>, 2018.

1133 Ji, D., Wang, L., Feng, J., Wu, Q., Cheng, H., Zhang, Q., Yang, J., Dong, W., Dai, Y.,

1134 Gong, D., Zhang, R.-H., Wang, X., Liu, J., Moore, J. C., Chen, D., and Zhou, M.:  
 1135 Description and basic evaluation of Beijing Normal University Earth System Model  
 1136 (BNU-ESM) version 1, *Geosci. Model Dev.*, 7, 2039–2064,  
 1137 <https://doi.org/10.5194/gmd-7-2039-2014>, 2014.

1138 Jin, H., Chen, X., Zhong, R., and Liu, M.: Influence and prediction of PM<sub>2.5</sub> through  
 1139 multiple environmental variables in China, *Sci. Total Environ.*, 849, 157910,  
 1140 <https://doi.org/10.1016/j.scitotenv.2022.157910>, 2022.

1141 Jones, A. C., Hawcroft, M. K., Haywood, J. M., Jones, A., Guo, X., Moore, J.C.:  
 1142 Regional climate impacts of stabilizing global warming at 1.5 K using solar  
 1143 geoengineering, *Earth's Future*, 6, <https://doi.org/10.1002/2017EF000720>, 2018.

1144 Kim, D. H., Shin, H. J., Chung, I. U.: Geoengineering: Impact of marine cloud  
 1145 brightening control on the extreme temperature change over East Asia, *Atmosphere*,  
 1146 11(12), 1345, <https://doi.org/10.3390/atmos11121345>, 2020.

1147 Klimont, Z., Kupiainen, K., Heyes, C., Purohit, P., Cofala, J., Rafaj, P., Borken-Kleefeld,  
 1148 J., and Schöpp, W.: Global anthropogenic emissions of particulate matter including  
 1149 black carbon, *Atmos. Chem. Phys.*, 17, 8681–8723, [https://doi.org/10.5194/acp-17-](https://doi.org/10.5194/acp-17-8681-2017)  
 1150 [8681-2017](https://doi.org/10.5194/acp-17-8681-2017), 2017.

1151 Kong, Q., and Huber, M.: Explicit calculations of wet-bulb globe  
 1152 temperature compared with approximations and why it matters for labor productivity,  
 1153 *Earth's Future*, 10, e2021EF002334, <https://doi.org/10.1029/2021EF002334>,  
 1154 2022.

1155 Kraaijenbrink, P. D. A., Bierkens, M. F. P., Lutz A. F., Immerzeel, W. W.:  
 1156 Impact of a global temperature rise of 1.5 degrees Celsius on Asia's glaciers, *Nature*,  
 1157 549, 257-260, <https://doi.org/10.1038/nature23878>, 2017.

1158 Kravitz, B., MacMartin, D., and Caldeira, K.: Geoengineering: Whiter skies?, *Geophys.*  
 1159 *Res. Lett.*, 39, L11801, <https://doi.org/10.1029/2012GL051652>, 2012.

1160 Kravitz, B., Robock, A., Boucher, O., Schmidt, H., Taylor, K. E., Stenchikov, G., and  
 1161 Schulz, M.: The geoengineering model intercomparison project (GeoMIP), *Atmos.*  
 1162 *Sci. Lett.*, 12(2), 162-167, <https://doi.org/10.1002/asl.316>, 2011.

1163 Kuswanto, H., Kravitz, B., Miftahurrohman, B., Fauzi, F., Sopahaluwaken, A., and  
 1164 Moore, J. C.: Impact of solar geoengineering on temperatures over the Indonesian  
 1165 Maritime Continent, *Int. J. Climatol.*, 1-20, <https://doi.org/10.1002/joc.7391>, 2021.

1166 Lee, C. and Sheridan, S.: A new approach to modeling temperature-related mortality:  
 1167 non-linear autoregressive models with exogenous input, *Environ. Res.*, 164:53–64,  
 1168 <https://doi.org/10.1016/j.envres.2018.02.020>, 2018.

1169 Lenton, T. and Vaughan, N.: The radiative forcing potential of different climate  
 1170 geoengineering options, *Atmos. Chem. Phys.*, 9, 5539–5561,  
 1171 <https://doi.org/10.5194/acp-9-5539-2009>, 2009.

1172 Li, D., Wu, Q., Feng, J., Wang, Y., Wang, L., Xu, Q., Sun, Y., Cao, K., and Cheng, H.:  
 1173 The influence of anthropogenic emissions on air quality in Beijing-Tianjin-Hebei of  
 1174 China around 2050 under the future climate scenario, *J. Cleaner Prod.*, 388, 135927,  
 1175 <https://doi.org/10.1016/j.jclepro.2023.135927>, 2023.

1176 Li, J., Chen, H., Li, Z., Wang, P., Cribb, M., and Fan, X.: Low-level temperature  
 1177 inversions and their effect on aerosol condensation nuclei concentrations under  
 different large-scale synoptic circulations, *Adv. Atmos. Sci.*, 32, 898-908,  
<https://doi.org/10.1007/s00376-014-4150-z>, 2015.

1178 Li, J., Chen, Y., Gan, T., Lau, N.: Elevated increases in human-perceived temperature  
1179 under climate warming, *Nat. Clim. Chang.*, 8 (1), 43–47,  
1180 <https://doi.org/10.1038/s41558-017-0036-2>, 2018.

1181 Li, K., Liao, H., Zhu, J., and Moch, J.: Implications of RCP emissions on future PM<sub>2.5</sub>  
1182 air quality and direct radiative forcing over China, *J. Geophys. Res. Atmos.*, 121, 12,  
1183 985–13, 008, <https://doi.org/10.1002/2016JD025623>, 2016.

1184 Li, M., Klimont, Z., Zhang, Q., Martin, R. V., Zheng, B., Heyes, C., Cofala, J., Zhang,  
1185 Y., and He, K.: Comparison and evaluation of anthropogenic emissions of SO<sub>2</sub> and  
1186 NO<sub>x</sub> over China, *Atmos. Chem. Phys.*, 18, 3433–3456, <https://doi.org/10.5194/acp-18-3433-2018>, 2018.

1188 Liao, T., Wang, S., Ai, J., Gui, K., Duan, B., Zhao, Q., Zhang, X., Jiang, W., and Sun, Y.:  
1189 Heavy pollution episodes, transport pathways and potential sources of PM<sub>2.5</sub> during  
1190 the winter of 2013 in Chengdu (China), *Sci. Total Environ.*, 584–585, 1056–1065,  
1191 <https://doi.org/10.1016/j.scitotenv.2017.01.160>, 2017.

1192 Lin, G., Fu, J., Jiang, D., Wang, J., Wang, Q., and Dong, D.: Spatial variation of the  
1193 relationship between PM<sub>2.5</sub> concentrations and meteorological parameters in China,  
1194 *BioMed Res. Int.*, 2015, 684618, <https://doi.org/10.1155/2015/684618>, 2015.

1195 Lo, J., Lau, A., Fung, J., and Chen, F.: Investigation of enhanced cross-city transport and  
1196 trapping of air pollutants by coastal and urban land-sea breeze circulations, *J.*  
1197 *Geophys. Res.-Atmos.*, 111(D14), <https://doi.org/10.1029/2005JD006837>, 2006.

1198 Luo, M., & Lau, N.-C.: Characteristics of summer heat stress in China during 1979–2014:  
1199 Climatology and long-term trends, *Climate Dynamics*, 53(9), 5375–5388,  
1200 <https://doi.org/10.1007/s00382-019-04871-5>, 2019.

1201 Luo, M. and Lau, N.: Increasing Human-Perceived Heat Stress Risks Exacerbated by  
1202 Urbanization in China: A Comparative Study Based on Multiple Metrics, *Earth’s*  
1203 *Future*, 9 (7), <https://doi.org/10.1029/2020EF001848>, 2021.

1204 Lyon, B. and Barnston, A.: Diverse characteristics of US summer heat waves, *J. Clim.*,  
1205 30 (19), 7827–7845, <https://doi.org/10.1175/JCLI-D-17-0098.1>, 2017.

1206 Maji, K., Ye, W., Arora, M., and Nagendra, S.: PM<sub>2.5</sub>-related health and economic loss  
1207 assessment for 338 Chinese cities, *Environ. Int.*, 121, 392–403,  
1208 <https://doi.org/10.1016/j.envint.2018.09.024>, 2018.

1209 Matthews, T., Wilby, R., and Murphy, C.: Communicating the deadly consequences of  
1210 global warming for human heat stress, *PNAS*, 114, 3861–3866,  
1211 <https://doi.org/10.1073/pnas.1617526114>, 2017.

1212 Miao, L., Moore, J. C., Zeng, F., Lei, J., Ding, J., He, B., and Cui, X.: Footprint of  
1213 research in desertification management in China, *Land Degrad. Dev.*, 26, 450–457,  
1214 <https://doi.org/10.1002/ldr.2399>, 2015.

1215 Mishra, D., Goyal, P., and Upadhyay, A.: Artificial intelligence based approach to  
1216 forecast PM<sub>2.5</sub> during haze episodes: a case study of Delhi, India, *Atmos. Environ.*,  
1217 102, 239–248, <https://doi.org/10.1016/j.atmosenv.2014.11.050>, 2015.

1218 Murray, F.: On the computation of saturation vapor pressure, Rand Corp Santa Monica  
1219 Calif, 1966.

1220 Nguyen, G., Shimadera, H., Uranishi, K., Matsuo, T., and Kondo, A.: Numerical  
1221 assessment of PM<sub>2.5</sub> and O<sub>3</sub> air quality in Continental Southeast Asia: Impacts of

1222 future projected anthropogenic emission change and its impacts in combination with  
1223 potential future climate change impacts, *Atmos. Environ.*, 226, 117398,  
1224 <https://doi.org/10.1016/j.atmosenv.2020.117398>, 2020.

1225 Perkins, S. and Alexander, L.: On the measurement of heat waves, *J Clim.*, 26 (13),  
1226 4500–4517, <https://doi.org/10.1175/JCLI-D-12-00383.1>, 2013.

1227 Ran, Q., Lee, S., Zheng, D., Chen, H., Yang, S., Moore, J., Dong, W.: Potential Health  
1228 and Economic Impacts of Shifting Manufacturing from China to Indonesia or India,  
1229 *Science of the total environment*, 855, 158634,  
1230 <http://dx.doi.org/10.1016/j.scitotenv.2022.158634>, 2022.

1231 Riahi, K., Rao, S., Krey, V., Cho, C., Chirkov, V., Fischer, G., Kindermann, G.,  
1232 Nakicenovic, N., Rafaj, P.: RCP 8.5—A scenario of comparatively high greenhouse  
1233 gas emissions, *Climatic Change* 109, 33, [https://doi.org/10.1007/s10584-011-0149-](https://doi.org/10.1007/s10584-011-0149-y)  
1234 [y](https://doi.org/10.1007/s10584-011-0149-y), 2011.

1235 Robock, A., Marquardt, A., Kravitz, B. and Stenchikov, G.: Benefits, risks, and costs of  
1236 stratospheric geoengineering, *Geophys. Res. Lett.*, 36(19),  
1237 <https://doi.org/10.1029/2009GL039209>, 2009.

1238 Shepherd, J.: Geoengineering the climate: Science, governance, and uncertainty, Royal  
1239 Society Policy document 10/09, 82 pp, 2009.

1240 Song, F., Zhang, G., Ramanathan, V. and Ruby Leung, L.: Trends in surface equivalent  
1241 potential temperature: A more comprehensive metric for global warming and  
1242 weather extremes, *Proc. Natl. Acad. Sci. U.S.A.*, 119, 6,  
1243 <https://doi.org/10.1073/pnas.2117832119>, 2022.

1244 Steadman, R. G.: A universal scale of apparent temperature, *J. Appl. Meteorol.*, 23 (12),  
1245 1674–1687, [https://doi.org/10.1175/1520-0450\(1984\)023<1674:AUSOAT>2.](https://doi.org/10.1175/1520-0450(1984)023<1674:AUSOAT>2.0.CO;2)  
1246 [0.CO;2](https://doi.org/10.1175/1520-0450(1984)023<1674:AUSOAT>2.0.CO;2), 1984.

1247 Steadman, R. G.: Norms of apparent temperature in Australia, *Aust. Meteorol. Mag.*, 43,  
1248 1–16, 1994.

1249 Stohl, A., Aamaas, B., Amann, M., Baker, L. H., Bellouin, N., Berntsen, T. K., Boucher,  
1250 O., Cherian, R., Collins, W., Daskalakis, N., Dusinska, M., Eckhardt, S., Fuglestvedt,  
1251 J. S., Harju, M., Heyes, C., Hodnebrog, Ø., Hao, J., Im, U., Kanakidou, M., Klimont,  
1252 Z., Kupiainen, K., Law, K. S., Lund, M. T., Maas, R., MacIntosh, C. R., Myhre, G.,  
1253 Myriokefalitakis, S., Olivié, D., Quaas, J., Quennehen, B., Raut, J.-C., Rumbold, S.  
1254 T., Samset, B. H., Schulz, M., Seland, Ø., Shine, K. P., Skeie, R. B., Wang, S., Yttri,  
1255 K. E., and Zhu, T.: Evaluating the climate and air quality impacts of short-lived  
1256 pollutants, *Atmos. Chem. Phys.*, 15, 10529–10566, [https://doi.org/10.5194/acp-15-](https://doi.org/10.5194/acp-15-10529-2015)  
1257 [10529-2015](https://doi.org/10.5194/acp-15-10529-2015), 2015.

1258 Su, J., Brauer, M., Ainslie, B., Steyn, D., Larson, T., and Buzzelli, M.: An innovative land  
1259 use regression model incorporating meteorology for exposure analysis, *Sci. Total*  
1260 *Environ.*, 390, 520-529, <https://doi.org/10.1016/j.scitotenv.2007.10.032>, 2008.

1261 Tong, C., Yim, S., Rothenberg, D., Wang, C., Lin, C., Chen, Y., and Lau, N.: Projecting  
1262 the impacts of atmospheric conditions under climate change on air quality over the  
1263 Pearl River Delta region, *Atmos. Environ.*, 193, 79-87,  
1264 <https://doi.org/10.1016/j.atmosenv.2018.08.053>, 2018.

1265 Torma, C. and Giogi, F.: Assessing the contribution of different factors in regional

1266 climate model projections using the factor separation method, *Atmos. Sci. Lett.*, 15,  
1267 239–244, <https://doi.org/10.1002/asl2.491>, 2014.

1268 Upadhyay, A., Dey, S., Goyal, P., and Dash, S.: Projection of near-future anthropogenic  
1269 PM<sub>2.5</sub> over India using statistical approach, *Atmos. Environ.*, 186, 178-188,  
1270 <https://doi.org/10.1016/j.atmosenv.2018.05.025>, 2018.

1271 Vandyck, T., Keramidas, K., Saveyn, B., et al.: A global stocktake of the Paris pledges:  
1272 Implications for energy systems and economy, *Global Environmental Change*, 41,  
1273 46-63, <https://doi.org/10.1016/j.gloenvcha.2016.08.006>, 2016.

1274 Wang, J., Allen, D., Pickering, K., Li, Z., He, H.: Impact of aerosol direct effect on East  
1275 Asian air quality during the EAST-AIRE campaign, *J. Geophys. Res.- Atmos.*, 121,  
1276 6534-6554, <https://doi.org/10.1002/2016JD025108>, 2016.

1277 Wang, J., Moore, J. C., Zhao, L., Yue, C., and Di, Z.: Regional dynamical and statistical  
1278 downscaling temperature, humidity and windspeed for the Beijing region under  
1279 stratospheric aerosol injection geoengineering, *Earth Syst. Dynam.*,  
1280 <https://doi.org/10.5194/esd-2022-35>, 2022.

1281 Wang, J., Feng, J., Yan, Z., Hu, Y., and Jia, G.: Nested high-resolution modeling of the  
1282 impact of urbanization on regional climate in three vast urban agglomerations in  
1283 China, *J. Geophys. Res.- Atmos.*, 117(D21), <https://doi.org/10.1029/2012JD018226>,  
1284 2017.

1285 Wang, J., Zhang, L., Niu, X., and Liu, Z.: Effects of PM<sub>2.5</sub> on health and economic loss:  
1286 Evidence from Beijing-Tianjin-Hebei region of China, *J. Cleaner Prod.*, 257, 120605,  
1287 <https://doi.org/10.1016/j.jclepro.2020.120605>, 2020.

1288 Wang, P., Luo, M., Liao, W., Xu, Y., Wu, S., Tong, X., Tian, H., Xu, F., Han, Y.:  
1289 Urbanization contribution to human perceived temperature changes in major urban  
1290 agglomerations of China, *Urban Climate*, 38, 100910,  
1291 <https://doi.org/10.1016/j.uclim.2021.100910>, 2021.

1292 Wang, S., Ancell, B., Huang, G., Baetz, B.: Improving robustness of hydrologic  
1293 ensemble predictions through probabilistic pre- and post-processing in sequential  
1294 data assimilation, *Water Resources Research*, 54, 2129–2151,  
1295 <https://doi.org/10.1002/2018WR022546>, 2018.

1296 Wang, X., Huang, G., Lin, Q., Nie, X., Cheng, G., Fan, Y., Li, Z., Yao, Y., Suo, M.: A  
1297 stepwise cluster analysis approach for downscaled climate projection - a Canadian  
1298 case study, *Environ. Model Softw.*, 49, 141–151,  
1299 <https://doi.org/10.1016/j.envsoft.2013.08.006>, 2013.

1300 Wang, Y., Hu, J., Zhu, J., Li, J., Qin, M., Liao, H., Chen, K., and Wang, M.: Health  
1301 Burden and economic impacts attributed to PM<sub>2.5</sub> and O<sub>3</sub> in China from 2010 to 2050  
1302 under different representative concentration pathway scenarios, *Resour. Conserv.  
1303 Recy.*, 173, 105731, <https://doi.org/10.1016/j.resconrec.2021.105731>, 2021.

1304 Wang, Y., Chen, L., Song, Z., Huang, Z., Ge, E., Lin, L., Luo, M.: Human-perceived-  
1305 temperature changes over South China: long-term trends and urbanization effects,  
1306 *Atmos. Res.*, 215, 116–127, <https://doi.org/10.1016/j.atmosres.2018.09.006>, 2019.

1307 Wang, Y., Yao, L., Wang, L., Liu, Z., Ji, D., Tang, G., Zhang, J., Sun, Y., Hu, N., and Xin,  
1308 J.: Mechanism for the formation of the January 2013 heavy haze pollution episode  
1309 over central and eastern China, *Sci. China Earth Sci.*, 57, 14-25,

1310 <https://doi.org/10.1007/s11430-013-4773-4>, 2014.

1311 Wang, Y., Zhuang, G., Zhang, X., Huang, K., Xu, C., Tang, A., Chen, J., and An, Z.: The  
1312 ion chemistry, seasonal cycle, and sources of PM<sub>2.5</sub> and TSP aerosol in Shanghai,  
1313 *Atmos. Environ.*, 40, 2935-2952, <https://doi.org/10.1016/j.atmosenv.2005.12.051>,  
1314 2006.

1315 Watanabe, S., Hajima, T., Sudo, K., Nagashima, T., Takemura, T., Okajima, H., Nozawa,  
1316 T., Kawase, H., Abe, M., Yokohata, T., Ise, T., Sato, H., Kato, E., Takata, K., Emori,  
1317 S., and Kawamiya, M.: MIROC-ESM 2010: model description and basic results of  
1318 CMIP5-20c3m experiments, *Geosci. Model Dev.*, 4, 845–872,  
1319 <https://doi.org/10.5194/gmd-4-845-2011>, 2011.

1320 Wei, J., Li, Z., Lyapustin, A., Sun, L., Peng, Y., Xue, W., Su, T., and Cribb, M.:  
1321 Reconstructing 1-km-resolution high-quality PM<sub>2.5</sub> data records from 2000 to 2018  
1322 in China: spatiotemporal variations and policy implications, *Remote Sens. Environ.*,  
1323 252, 112136, <https://doi.org/10.1016/j.rse.2020.112136>, 2021.

1324 Wilcke, R. A. I., Mendlik, T., Gobiet, A.: Multi-variable error correction of regional  
1325 climate models, *Clim. chang.*, 120(4), 871-887, <https://doi.org/10.1007/s10584-013-0845-x>, 2013.

1327 Wu, D., Tie, X., Li, C., Ying, Z., Kai-Hon Lau, A., Huang, J., Deng, X., and Bi, X.: An  
1328 extremely low visibility event over the Guangzhou region: a case study, *Atmos.*  
1329 *Environ.*, 39, 6568-6577, <https://doi.org/10.1016/j.atmosenv.2005.07.061>, 2005.

1330 Wu, J., Gao, X., Giorgi, F., Chen, D.: Changes of effective temperature and cold/hot days  
1331 in late decades over China based on a high resolution gridded observation dataset,  
1332 *Int. J. Climatol.*, 37:788–800, <https://doi.org/10.1002/joc.5038>, 2017.

1333 Xu, J., Yao, M., Wu, W., Qiao, X., Zhang, H., Wang, P., Yang, X., Zhao, X., and Zhang,  
1334 J.: Estimation of ambient PM<sub>2.5</sub>-related mortality burden in China by 2030 under  
1335 climate and population change scenarios: A modeling study, *Environ. Int.*,  
1336 156,106733, <https://doi.org/10.1016/j.envint.2021.106733>, 2021.

1337 Xue, W., Zhang, J., Zhong, C., Li, X., and Wei, J.: Spatiotemporal PM<sub>2.5</sub> variations and  
1338 its response to the industrial structure from 2000 to 2018 in the Beijing-Tianjin-  
1339 Hebei region, *J. Cleaner Prod.*, 279, 123742,  
1340 <https://doi.org/10.1016/j.jclepro.2020.123742>, 2021.

1341 Yang, S., Ma, Y., Duan, F., He, K., Wang, L., Wei, Z., Zhu, L., Ma, T., Li, H., Ye, S.:  
1342 Characteristics and formation of typical winter haze in Handan, one of the most  
1343 polluted cities in China, *Sci. Total Environ.*, 613-614, 1367-1375,  
1344 <https://doi.org/10.1016/j.scitotenv.2017.08.033>, 2018.

1345 Yang, X., Wu, Q., Zhao, R., Cheng, H., He, H., Ma, Q., Wang, L., and Luo, H.: New  
1346 method for evaluating winter air quality: PM<sub>2.5</sub> assessment using Community  
1347 Multiscale Air Quality Modeling (CMAQ) in Xi'an, *Atmos. Environ.*, 211, 18-28,  
1348 <https://doi.org/10.1016/j.atmosenv.2019.04.019>, 2019.

1349 Yang, X., Zhao, C., Guo, J., and Wang, Y.: Intensification of aerosol pollution associated  
1350 with its feedback with surface solar radiation and winds in Beijing, *J. Geophys. Res.*  
1351 *Atmos.*, 121, 4093-4099, <https://doi.org/10.1002/2015JD024645>, 2016.

1352 Yang, Y., Maraun, D., Ossó, A., and Tang, J.: Increased spatial extent and likelihood of  
1353 compound long-duration dry and hot events in China, 1961–2014, *Nat. Hazards*



1354 Earth Syst. Sci., 23, 693–709, <https://doi.org/10.5194/nhess-23-693-2023>, 2023.

1355 Yang, Y., and Tang, J.: Substantial Differences in Compound Long - Duration Dry and  
 1356 Hot Events Over China Between Transient and Stabilized Warmer Worlds at 1.5° C  
 1357 Global Warming, *Earths Future*, 11, e2022EF002994,  
 1358 <https://doi.org/10.1029/2022EF002994>, 2023.

1359 Yang, Y., Tang, J., Xiong, Z., Wang, S., and Yuan, J.: An intercomparison of multiple  
 1360 statistical downscaling methods for daily precipitation and temperature over China:  
 1361 future climate projections, *Clim. Dynam.*, 52, 6749–  
 1362 6771, <https://doi.org/10.1007/s00382-018-4543-2>, 2019.

1363 Yin, Z., Wang, H., and Chen, H.: Understanding severe winter haze events in the North  
 1364 China Plain in 2014: roles of climate anomalies, *Atmos. Chem. Phys.*, 17, 1641–  
 1365 1651, <https://doi.org/10.5194/acp-17-1641-2017>, 2017.

1366 You, T., Wu, R., Huang, G., Fan, G.: Regional meteorological patterns for heavy  
 1367 pollution events in Beijing, *J. Meteorolog. Res.*, 31, 597-611,  
 1368 <https://doi.org/10.1007/s13351-017-6143-1>, 2017.

1369 Yu, X., Moore, J. C., Cui, X., Rinke, A., Ji, D., Kravitz, B., and Yoon, J.: Impacts,  
 1370 effectiveness and regional inequalities of the GeoMIP G1 to G4 solar radiation  
 1371 management scenarios, *Global and Planetary Change*, 129, 10-22,  
 1372 <https://doi.org/10.1016/j.gloplacha.2015.02.010>, 2015.

1373 Zhan, P., Zhu, W., Zhang, T., Cui, X., Li, N.: Impacts of sulfate geoengineering on rice  
 1374 yield in China: Results from a multimodel ensemble, *Earth's Future*, 7(4), 395-410,  
 1375 <https://doi.org/10.1029/2018EF001094>, 2019.

1376 Zhang, Q., Zheng, Y., Tong, D., Shao, M., Wang, S., Zhang, Y., Xu, X., Wang, J., He, H.,  
 1377 Liu, W., Ding, Y., Lei, Y., Li, J., Wang, Z., Zhang, X., Wang, Y., Cheng, J., Liu, Y.,  
 1378 Shi, Q., Yan, L., Geng, G., Hong, C., Li, M., Liu, F., Zheng, B., Cao, J., Ding, A.,  
 1379 Gao, J., Fu, Q., Huo, J., Liu, B., Liu, Z., Yang, F., He, K., and Hao, J.: Drivers of  
 1380 improved PM<sub>2.5</sub> air quality in China from 2013 to 2017, *PNAS*, 116, 24463-24469,  
 1381 <https://doi.org/10.1073/pnas.1907956116>, 2019.

1382 Zhang, Z., Gong, D., Mao, R., Kim, S., Xu, J., Zhao, X., and Ma, Z.: Cause and  
 1383 predictability for the severe haze pollution in downtown Beijing in November–  
 1384 December 2015, *Sci. Total Environ.*, 592, 627-638,  
 1385 <https://doi.org/10.1016/j.scitotenv.2017.03.009>, 2017.

1386 Zhao, D., Xin, J., Gong, C., Quan, J., Liu, G., Zhao, W., Wang, Y., Liu, Z., and Song, T.:  
 1387 The formation mechanism of air pollution episodes in Beijing city: insights into the  
 1388 measured feedback between aerosol radiative forcing and the atmospheric boundary  
 1389 layer stability, *Sci. Total Environ.*, 692, 371–381,  
 1390 <https://doi.org/10.1016/j.scitotenv.2019.07.255>, 2019.

1391 Zheng, C., Zhao, C., Zhu, Y., Wang, Y., Shi, X., Wu, X., Chen, T., Wu, F., and Qiu, Y.:  
 1392 Analysis of influential factors for the relationship between PM<sub>2.5</sub> and AOD in  
 1393 Beijing, *Atmos. Chem. Phys.*, 17, 13473–13489, <https://doi.org/10.5194/acp-17-13473-2017>, 2017.

1395 Zhou, B., Xu, Y., Wu, J., Dong, S., and Shi, Y.: Changes in temperature and precipitation  
 1396 extreme indices over China: analysis of a high-resolution grid dataset, *Int. J.*  
 1397 *Climatol.*, 36, 1051–1066, <https://doi.org/10.1002/joc.4400>, 2016.

1398 Zhu, J., Wang, S., Huang, G.: Assessing Climate Change Impacts on Human-Perceived  
1399 Temperature Extremes and Underlying Uncertainties, *Journal of Geophysical*  
1400 *Research: Atmosphere*, 124 (7), 3800-3821, <https://doi.org/10.1029/2018JD029444>,  
1401 2019.

1402 Zhu, X., Huang, G., Zhou, X., Zheng, S.: Projection of apparent temperature using  
1403 statistical downscaling approach in the Pearl River Delta, *Theor. Appl. Climatol.*,  
1404 144 (3–4), 1253–1266, <https://doi.org/10.1007/s00704-021-03603-2>, 2021.

1405